OXFORD

Journal of Petrology, 2022, **63**, 1–18
https://doi.org/10.1093/petrology/egac111
Original Manuscript

Effects of Mantle Hybridization by Interaction with Slab Derived Melts in the Genesis of Alkaline Lavas across the Back-Arc Region of South Shetland Subduction System

Şafak Altunkaynak [1], Ercan Aldanmaz [2] and Daniel Nývlt[3,4]

[1]Department of Geological Engineering, Istanbul Technical University, Maslak 34469, Istanbul, Turkey
[2]Department of Geology, University of Kocaeli, 41380 Izmit, Turkey
[3]Department of Geography, Faculty of Science, Masaryk University, Kotlářská 2, 611 37 Brno, Czech Republic
[4]Czech Geological Survey, Brno branch, Leitnerova 22, 658 69 Brno, Czech Republic

*Corresponding author. safak@itu.edu.tr

Abstract

Late Miocene to Late Pleistocene alkaline lavas in the northernmost part of the Antarctic Peninsula and its off-lying islands are the latest stage of magmatic activity that took place in response to lithospheric extension in the back-arc region of the South Shetland subduction system. The alkaline magmatism occurred much later than the main pulse of Cretaceous arc magmatism and generated basaltic extrusive rocks during several sub-aqueous/sub-glacial and sub-aerial eruption periods. The suite consists primarily of alkali olivine basalts with oceanic island basalt (OIB)-like trace element signatures, characterized by elevated highly to less incompatible element ratios compared to MORB. The samples have higher $^{87}Sr/^{86}Sr$ (0.70301–0.70365), and lower $^{143}Nd/^{144}Nd$ (0.51283–0.51294) and $^{176}Hf/^{177}Hf$ (0.28291–0.28298) than depleted MORB mantle. Their lead isotope ratios vary within a limited range with $^{206}Pb/^{204}Pb$, $^{207}Pb/^{204}Pb$, $^{208}Pb/^{204}Pb$ ratios of 18.797–18.953, 15.577–15.634, and 38.414–38.701, respectively. Sr, Nd, Hf and Pb isotope systematics suggest involvement of diverse source materials in the genesis of the alkaline magmas. Evaluation of radiogenic isotope and trace element data indicates that the source of the alkaline melts had a complex petrogenetic history, reflecting the effects of mantle hybridization along the slab mantle interface through interaction of mantle wedge peridotites with volatile-bearing, siliceous melts produced by melting of subducted sediments and basaltic oceanic crust. Hf-Nd isotope and trace element projections further demonstrate that the metasomatizing melt was likely generated by eclogite partial melting at sub-arc to post-arc depths, in equilibrium with a garnet-bearing residue and involved breakdown of high field strength elements (HFSE) retaining phases. Consumption of metasomatic amphibole during partial melting of hybridized peridotite at the wet solidus appears to have had a significant effect on the final melt compositions with high HFSE, Na and H_2O contents.

Keywords: Antarctic Peninsula, alkali magmatism, radiogenic isotopes, mantle source, petrogenesis

INTRODUCTION

Mantle-derived basaltic magmas with intraplate geochemical signatures commonly occur in back-arc settings and active continental margins (Briggs & McDonough, 1990; Tatsumi *et al.*, 2000; Aldanmaz *et al.*, 2006). These magmas are similar in composition to typical oceanic island basalts (OIB), characterized by high alkali contents and enrichments in highly incompatible trace elements compared to tholeiitic basalts erupted at mid-oceanic spreading centers. Their geochemical characteristics also differ from those of typical back-arc basin basalts (BABB; Taylor & Martinez, 2003) in that they possess unfractionated LILE/HFSE ratios, suggesting derivation from a source that lacks enrichment in fluid-mobile elements. However, their volatile contents are similar to arc-melts and are interpreted to reflect the imprints of mantle hydration, indicating derivation from subduction-influenced source regions (Liu *et al.*, 2015; Altunkaynak *et al.*, 2019).

The contrasting trace element behavior during the generation of different types of melts in subduction settings is generally attributed to variations in the metasomatizing agent released from the subducted slab over a range of pressures and temperatures (Ringwood, 1990; Gao *et al.*, 2007; Xiao *et al.*, 2012). Distinct trace element relative abundances of OIB and typical arc magmas in these settings are commonly interpreted to be the result of the diverse effects of hydrous melts vs. aqueous fluids originating from the slab at different depths (Hastie *et al.*, 2011; Kimura *et al.*, 2014; Zheng, 2019).

Alkaline magmatism with OIB geochemical signatures in extending active continental margins usually represents the latest stage of magmatic activity and generally occurs in rear-arc regions at some distance from the established magmatic arc (e.g. Briggs & McDonough, 1990; Brombin *et al.*, 2019; Elizondo-Pacheco *et al.*, 2022). Unlike typical arc magmas, which mainly originate from aqueous fluid flux-induced melting of wedge peridotites, the alkaline magmas appear to emerge from the passive upwelling of wet and/or hot mantle material from a deeper part of the mantle wedge in response to overriding plate extension (e.g. Ma & Xu, 2021). The incompatible trace element enriched nature of these magmas is generally attributed to hybridization of the source mantle by interaction with volatile-rich melts at

Received: June 29, 2022. **Revised:** October 18, 2022. **Accepted:** October 18, 2022

post-arc depths (Ringwood, 1990; Dai *et al.*, 2017; Zheng, 2019). The mechanisms that may contribute include metasomatism of the wedge peridotites through interaction with slab-derived hydrous silicate melts (Prouteau *et al.*, 2001; Hastie *et al.*, 2011) or carbonated eclogite-derived melts (Yaxley & Green, 1998; Mallik & Dasgupta, 2013; Rosenthal *et al.*, 2014). Such interactions can cause local compositional anomalies with fusible modal mineralogy (e.g. amphibole- or phlogopite-bearing peridotites), which eventually undergo pressure release partial melting during subsequent lithospheric extension (Liu *et al.*, 2015; Wang *et al.*, 2021).

The area between the Scotia Sea, the Weddell Sea and the Drake Passage in the Southern Ocean is a complex framework of tectonic plates in which several lithospheric fragments are moving relative to one another along convergent, divergent or transform plate boundaries (Barker, 2001; Eagles *et al.*, 2009). Magmatic activity occurred in response to the subduction of the Phoenix Plate beneath the South Shetlands Plate along the South Shetland Trench (Fig. 1). This resulted in development of a magmatic arc with abundant low-K tholeiitic to medium-K calc-alkaline eruptive products during the Cretaceous to Neogene period (130 to 20 Ma; Pankhurst & Smellie, 1983; Birkenmajer *et al.*, 1986).

Subsequent overriding plate extension caused the opening of the Bransfield Strait as an extensional marginal basin and led to widespread tholeiitic to alkaline magmatism during the Late Miocene to Late Pleistocene (<6.7 Ma; Smellie *et al.*, 2008) over a large area in the back-arc region (Fig. 1). Exposures of alkaline magmatic rocks are distributed across the northernmost part of the Antarctic Peninsula and its off-lying islands (Smellie, 1987; Hole *et al.*, 1995). Several periods of magmatic activity, characterized by both sub-aqueous/sub-glacial and sub-aerial eruptions, produced various pillow-structured basalt lavas and hyaloclastite breccias as well as sub-aerial lavas and local mafic intrusions (Smellie, 1987; Hole *et al.*, 1995; Smellie *et al.*, 2008; Altunkaynak *et al.*, 2018).

For the origin of these alkaline magmas, some previous studies proposed small degrees of partial melting of an enriched asthenosphere, with lithospheric extension as the main driving mechanism of melt production (Keller *et al.*, 1992; Hole *et al.*, 1995; Košler *et al.*, 2009). Others used the arc-melt-like volatile contents of the primary magmas to emphasize the significance of slab-derived components in generating a hydrated source in the mantle wedge (Altunkaynak *et al.*, 2019). Here, we present Sr, Nd, Hf and Pb isotope and trace element variations for the alkaline lavas from islands at the north-eastern tip of the Antarctic Peninsula, to explore the nature of their mantle source and provide constraints on the possible mechanisms that operated to form a within-plate magma source above the subducting Phoenix Plate. We particularly focus on modeling and interpretation of geochemical data to characterize the variations in the source chemistry in terms of trace element abundances and radiogenic isotope systematics and to understand the nature and composition of possible mantle end-member components. We emphasize the effects of the involvement of compositionally different slab material during mantle wedge hybridization.

GEOLOGICAL BACKGROUND

Subduction of the Phoenix Plate beneath the Antarctic Peninsula along the South Shetland Trench was initiated during the Mesozoic (Barker, 2001). Vertical displacements of the Antarctic–Phoenix Ridge axis by several NNW–SSE trending fracture zones gave rise to ridge segmentation and progressive elimination of the ridge segments, which caused the entire ridge system to become extinct (Larter & Barker, 1991; Livermore *et al.*, 2000). The remnant of the Phoenix Plate is separated from the Scotia Plate by the Shackleton Fracture Zone and from the Antarctic Plate by the Hero Fracture Zone.

After over 100 million years of active subduction (Larter & Barker, 1991), the subduction velocity of the Phoenix Plate decreased gradually. Recent GPS data suggest a present-day subduction rate of less than 1 cm a^{-1} (Robertson Maurice *et al.*, 2003), and some argue that subduction may even have ended completely (Livermore *et al.*, 2000). This caused slab steepening and rollback-induced lithospheric extension in the overriding Antarctic Plate. Lithospheric spreading was accommodated by rollback of the steepened Phoenix Plate in combination with sinistral transcurrent movement between the Antarctic and Scotia plates along the Shackleton Fracture Zone (Fretzdorff *et al.*, 2004) (Fig. 1).

Subduction of the Phoenix Plate underneath the Antarctic Plate built an active continental margin-type volcanic arc, consisting predominantly of low- to medium-K magmatic rocks along the South Shetland Islands and the Antarctic Peninsula. Located approximately 250 km southeast of the South Shetland Trench, the James Ross Archipelago in the north-eastern Antarctic Peninsula is a site of voluminous back-arc volcanism (e.g. Košler *et al.*, 2009; Smellie, 2021). Effusive eruptions of alkaline basaltic lavas formed a large volcanic field, covering more than 6000 km^2 and dominating the exposed geology of James Ross Island, Vega Island, and some other small islands in the Prince Gustav Channel and Antarctic Sound as well as the Trinity and Tabarin peninsulas of the Antarctic Peninsula (e.g. Smellie, 2021; Fig. 1).

The volcanic field was formed by episodic subglacial/lacustrine-marine and sub-aerial volcanic activity, and the products of this activity have been referred to as the James Ross Island Volcanic Group (JRIVG; Nelson, 1975). James Ross Island (2500 km^2), between latitude 63°45′ 64°30′S and longitude 58°30′ 57°00′W, displays the most prominent outcrop of this volcanic field (Fig. 1) where more than 50 effusive eruption phases have developed since the Late Miocene (Smellie *et al.*, 2008). James Ross Island and other smaller outcrops of JRIVG are built up from a major polygenetic shield volcano, Mt. Haddington (1630 m), extending ENE-WSW. The volcanic activity on these islands formed mainly as part of the initial stages of the sub-glacial/submarine basalt eruption of this volcano and the multiple satellite centers in the northern part of the island and surrounding small islands (Smellie *et al.*, 2008; Smellie, 2021). Many of the satellite centers are monogenic glacio-volcanic edifices. Vega Island, on the other hand, is a massive satellite volcanic shield (Smellie, 2021).

The JRIVG is made up of several pahoehoe lava-fed delta sequences, shallow intrusions, and a few Surtseyan tuff cones as well as Strombolian cinder cones that unconformably overlie the Mesozoic to Cenozoic sedimentary rocks of the James Ross Basin (Skilling, 2002; Nývlt *et al.*, 2011; Smellie *et al.*, 2013; Mlčoch *et al.*, 2020). Lava-fed delta sequences with thicknesses of 100 to 600 m (generally 100–250 m; Smellie *et al.*, 2008) consist mainly of four lithofacies: a- bottomset volcaniclastic/siliciclastic deposit of glaciogenic/marine origin (accompanied by pillow lavas and peperites in some localities), b- foreset-bedded hyaloclastite breccias, c- topset subaerial lava flows, and d- shallow intrusions (Fig. 2a-g) (Smellie *et al.*, 2008; Košler *et al.*, 2009; Nehyba & Nývlt, 2015; Altunkaynak *et al.*, 2018). Published K-Ar and Ar-Ar radiometric data reveal that the basaltic eruptions mainly occurred between 6.7 and < 0.13 Ma (Hole *et al.*, 1995; Kristjánsson

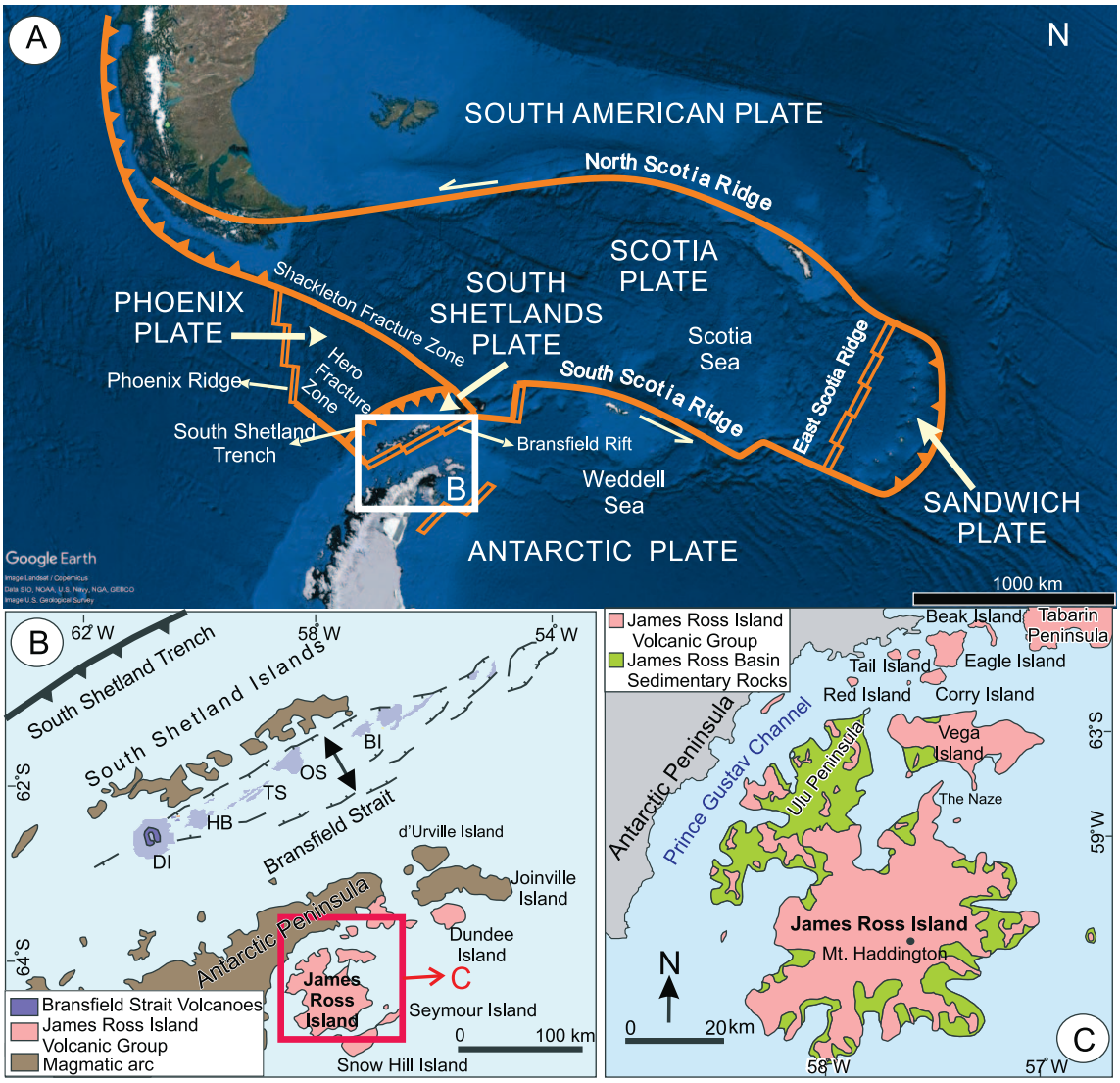

Fig. 1. Maps showing **a-** the plate reconstruction of the Scotia Sea region; **b-** the magmatic belts across the south Shetland Subduction Zone; and **c-** the distribution of JRIVG (modified from Elliot, 1988 and Smellie *et al.*, 2013). *Key to abbreviations:* DI: Deception Island; HB: Humpback Seamount; TS: Three Sisters Ridge; OS: Orca Seamount; BI: Bridgeman Island.

et al., 2005; Smellie *et al.*, 2008; Nývlt *et al.*, 2011; Nehyba & Nývlt, 2015).

SAMPLE DESCRIPTION

The investigated volcanic rocks are from pillow lavas, pillow lava fragments/blocks within the hyaloclastite breccias, subaerial lavas, and shallow intrusions. Most samples were collected from the Ulu and Naze peninsulas of James Ross Island (n = 20), while other sampling sites include Vega Island (Cape Lamb area) (n = 3), Eagle Island (n = 3), and Tail Island (n = 2) in the northeastern part of Prince Gustav Channel. Sampling localities are shown in Fig. 1 and listed in supplementary Table 1.

The lava samples are all basaltic and composed of phenocrysts of olivine and plagioclase with minor clinopyroxene set in a fine-grained groundmass consisting of plagioclase microlites with less abundant olivine and clinopyroxene. The pillow basalt samples are commonly porphyritic and show characteristic quenching textures (Fig. 3a). The groundmass may contain spherulitic growths of plagioclase and clinopyroxene (Fig. 3a). Olivine has skeletal interiors with glass inclusions (Fig. 3b). Quenching is also evident by the presence of dendritic Fe-Ti oxides (magnetite and ilmenite). Lava fragments in hyaloclastite breccias and lapilli tuffs show similar mineralogical and textural characteristics to the pillow basalts. Angular and subangular vitroclasts and pillow lava (hyalobasalt) fragments are partly or completely altered to a yellow-orange palagonite (Fig. 3c, d).

The samples from the intrusions are medium- to fine-grained olivine dolerites and olivine basalts that consist mainly of olivine, Ca-plagioclase and clinopyroxene. Dolerite intrusions are mostly holocrystalline and exhibit sub-ophitic to ophitic texture in which plagioclase laths are completely or partly enclosed by clinopyroxene (Fig. 3e). In their contacts with hyaloclastites, intrusions display quenched textures similar to pillow lavas.

The sub-aerial pahoehoe lavas have petrographic features similar to those of the pillow lavas except that they display no quench textures. They are mainly olivine-phyric basalts with plagioclase-rich fine-grained groundmass. Olivine is the most abundant phenocryst phase, accompanied by minor plagioclase and clinopyroxene. Some olivine phenocrysts have rounded and embayed

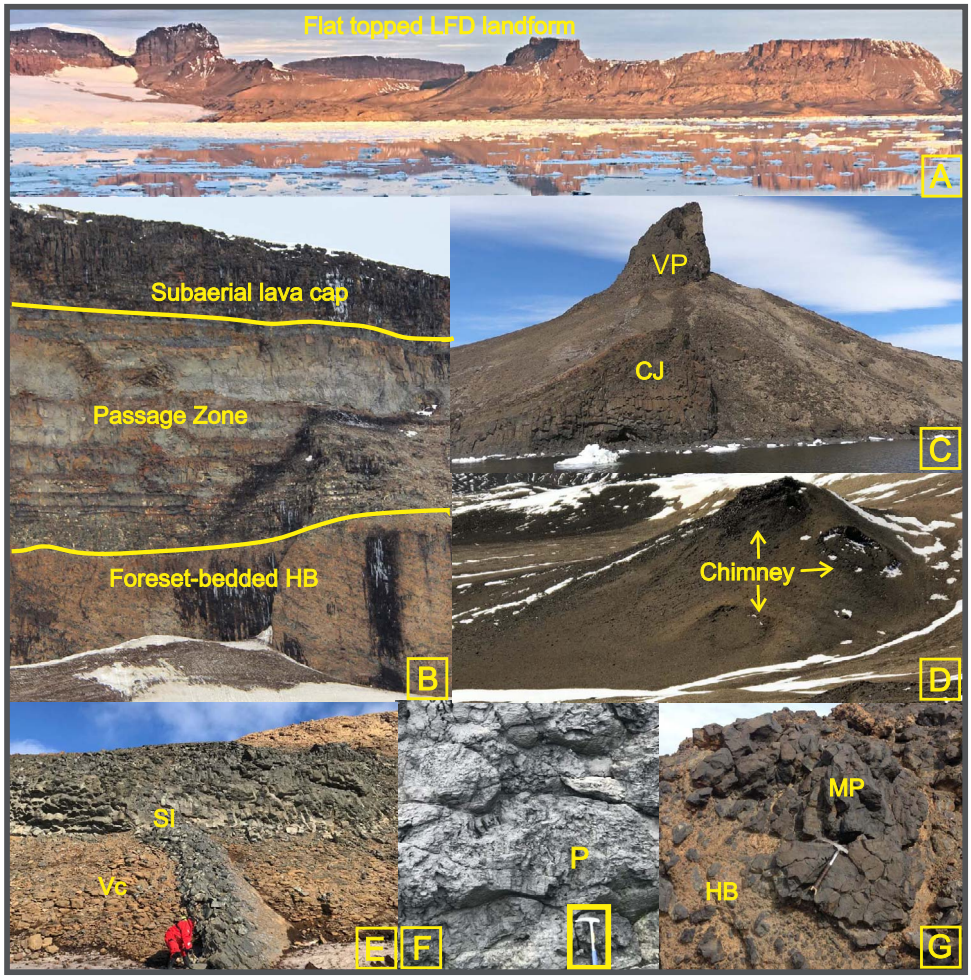

Fig. 2. a- Flat-topped Lava-Fed Delta (LFD) landform (Vega Island); **b-** LDF sequence in southern Lahman Craig (James Ross Island; JRI); **c-** Volcanic plug (VP) and radially fanning columnar jointing (CJ) in subglacial/marine basalt intrusion (The Naze, JRI); **d-** Basaltic Chimney (Stoneley Point, JRI); **e-** Shallow intrusion (SI) intruded into volcanoclastics (Vc) (Tail island); **f-** Corrugated closely packed pillow lavas (P) in Cape Lachman (JRI), g- Mega pillow (MP) within hyaloclastite breccia (HB) (The Naze, JRI).

edges. The groundmass is made up of microcrystalline plagioclase accompanied by lesser amounts of olivine and clinopyroxene. In some localities, the sub-aerial basaltic lavas contain ultramafic xenoliths and disaggregated olivine, which display undulose extinction, strain lamella, and reaction rims characterized by spongy textures (Fig. 3f).

BULK-ROCK GEOCHEMISTRY

Analytical procedures

Volcanic rock samples with no effects of weathering or alteration were selected for bulk-rock geochemical analyses. Rock powders were prepared by removing the external surfaces, crushing and then grinding in an agate ball mill. Major oxide abundances were measured on fused discs using X-ray fluorescence (XRF) at the ACME Analytical Laboratories in Vancouver, Canada. Loss on ignition was determined by heating a separate aliquot of rock powder at 900°C for >2 h. Trace element analyses were conducted at the Department of Geology, University of Kocaeli, Turkey. Rock powders were fused using lithium tetraborate ($Li_2B_4O_7$) to ensure complete dissolution and then dissolved in hot HF and HNO_3. Trace element abundances were measured using ICP-MS (Perkin Elmer Elan DRC-e). Reproducibility, based on repeated analyses of samples and standards (W-2 and AGV2), was better than 2% and 5% (RSD) for major and trace elements, respectively.

A representative subset of samples was selected for Sr, Nd, Hf and Pb isotope measurements. Analyses were performed using a Nu Plasma MC-ICP mass spectrometer at the G-Time Laboratory, Université Libre de Bruxelles (Belgium). The procedures applied are described in detail in Mata *et al.* (2017). Strontium isotope analyses were performed in wet plasma mode. Instrumental mass fraction was corrected by normalizing to $^{86}Sr/^{88}Sr = 0.1194$. Mass bias correction was made by repeated analyses of an in-house Sr standard solution, which was calibrated and normalized to the certified value of NBS 987 Sr standard ($^{86}Sr/^{88}Sr = 0.710248$) reported by Weis *et al.* (2006). During the analyses, the in-house standard solution was run between every two samples and gave an average value of $^{86}Sr/^{88}Sr$ of 0.710287 ± 50 (2SD, $N = 21$).

Neodymium and Hf isotope measurements were made in dry mode using an Aridus II desolvating nebulizer system. Instrumental mass bias was monitored by repeated analyses of samples and standards. During the analysis, the Rennes Nd standard gave $^{143}Nd/^{144}Nd$ of 0.511962 ± 12 (2SD, $N = 24$), while the JMC 475 Hf standard gave $^{176}Hf/^{177}Hf$ of 0.282164 ± 17 (2SD, $N = 20$). Neodymium and Hf isotope data were normalized to $^{146}Nd/^{144}Nd = 0.7219$ and $^{179}Hf/^{177}Hf = 0.7325$ and are reported

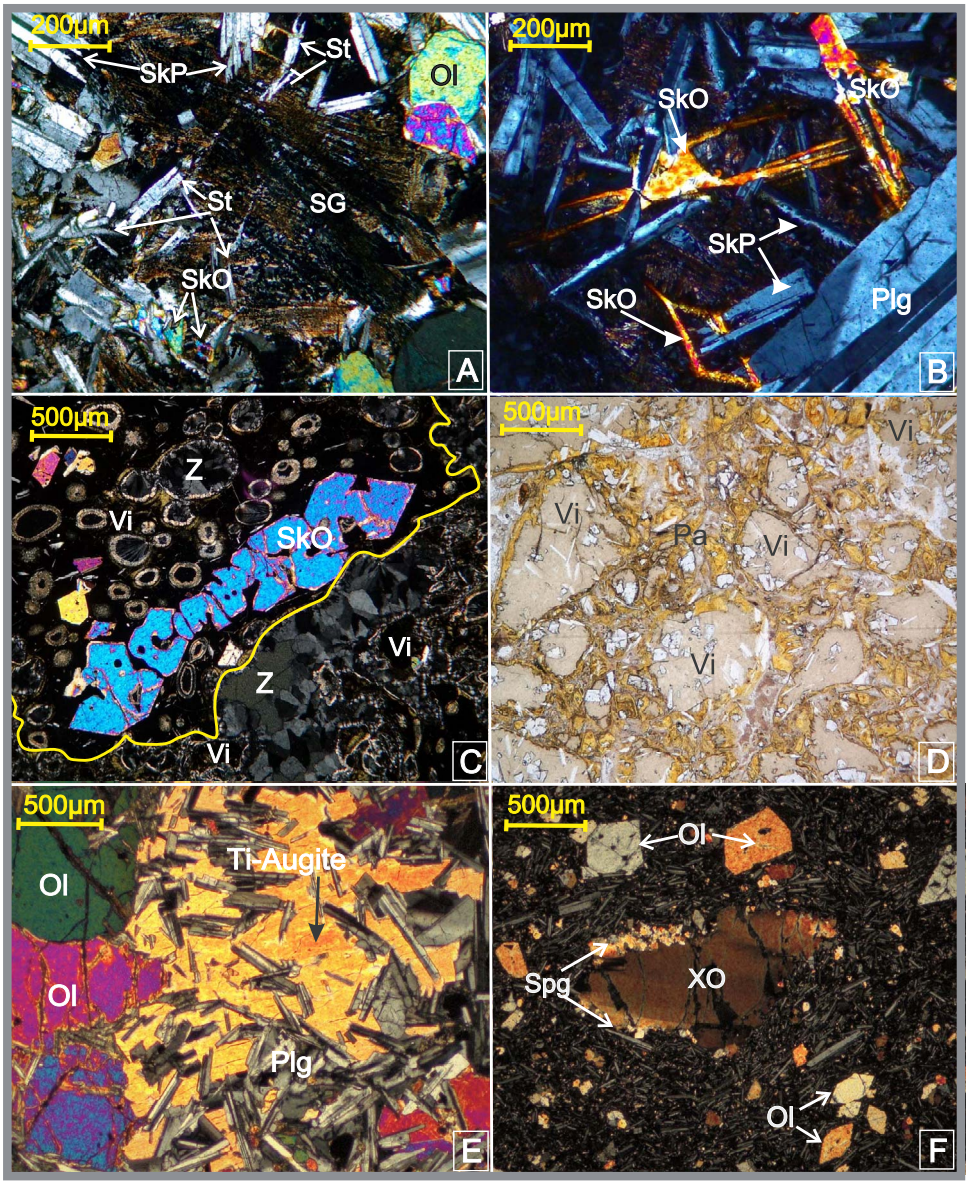

Fig. 3. Photomicrographs of JRIVG lavas and shallow intrusions; **a-** pillow basalt with quenched texture, Ulu Peninsula, James Ross Island (cross-polarized light; XPL, St: swallow-tailed plagioclase microlite, SkP: Skeletal Plagioclase, SkO: Skeletal olivine, SG: Spherolitic groundmass showing fan-shaped dendritic clinopyroxene and opaque minerals); **b-** Skeletal olivine (SkO) and plagioclase (SkP) microcrystals in megapillows; Lagun Mesa, James Ross Island (XPL); **c-** vitroclasts (Vi), Skeletal olivine (SkO) and zeolite (Z) filling amygdale within hyaloclastite breccia, The Naze, James Ross Island (XPL); **d-** Pale brown vitroclasts (Vi) rimmed by palagonite (Pa) in hyaloclastite, Tail Island (plane-polarized light; PPL); **e-** ophitic intergrown of Ti-augite and plagioclase(Plg) in olivine dolerite intrusion; Vega Island (XPL); **f-** xenocrystic olivine (XO) with spongy rim (Spg) and olivine (Ol) microphenocrysts set in pilotaxitic groundmass of subaerial olivine basalt; Eagle Island (XPL).

relative to the reference values of 0.511961 and 0.282160, respectively (Chauvel *et al.*, 2011).

Lead isotope measurements were performed using a thallium doped solutions with a constant lead/thallium concentration ratio of 5/1. The analyses were performed in wet plasma mode with a minimum ^{204}Pb signal intensity of 100 mV in the axial collector. The ^{202}Hg beam intensity was routinely monitored to correct for possible isobaric interference of ^{204}Hg on ^{204}Pb. Mass discrimination was monitored by external normalization through thallium doping and calibrator sample bracketing method using the certified values of NBS981 Pb standard ($^{206}Pb/^{204}Pb = 16.9405 \pm 15$; $^{207}Pb/^{204}Pb = 15.4963 \pm 16$; $^{208}Pb/^{204}Pb = 36.7219 \pm 44$; Galer & Abouchami, 1998). Repeated analyses of the NBS981 standard yielded the following ratios and associated 2SD uncertainties: $^{206}Pb/^{204}Pb = 16.9400 \pm 40$, $^{207}Pb/^{204}Pb = 15.4959 \pm 27$, $^{208}Pb/^{204}Pb = 36.7209 \pm 08$.

Major and trace elements

Major and selected trace element concentrations of the samples are listed in supplementary Table 1. The alkaline suite is composed of low-silica basaltic rocks with high MgO (5.02–10.17 wt.%) and total alkali ($K_2O + Na_2O = 4.29$–6.17 wt.%) contents. The rocks display limited SiO_2 compositional variations (45–49 wt.%) and have Mg# [cation proportion of $Mg/(Mg + Fe_{total})$] ranging between 0.53 and 0.69. The samples are mostly sodic alkaline, with Na_2O/K_2O ratios of 2.07–4.17, and have moderate TiO_2 (1.59–2.23 wt. %) and CaO (3.80–9.43 wt.%) and high Al_2O_3 (14.10–16.70 wt.%) contents. They are basalts and trachybasalts and

plot mostly in the alkaline field with only a few samples plotting close to the dividing line between the alkaline and sub-alkaline fields on a total alkali vs. silica diagram of Le Bas *et al.* (1986), indicating that the rocks are mildly to moderately alkaline (Fig. 4a). In comparison with the South Shetland island arc lavas (Machado *et al.*, 2005; Haase *et al.*, 2012), and the subalkaline lavas of the Bransfield Basin (Keller *et al.*, 2002; Fretzdorff *et al.*, 2004; Haase *et al.*, 2011), the alkaline rocks have distinctly higher total alkali and potassium contents (Fig. 4b). In terms of their alkali-silica variations, they display some similarities to the OIB-type intraplate lavas erupted along the West Antarctic rift system (Aviado *et al.*, 2015; Panter *et al.*, 2018) (Fig. 4).

The samples are characterized by relative enrichments in all highly incompatible elements compared to MORB compositions. On a multi-element diagram, the rocks exhibit strong enrichments in LILE, L-MREE and HFSE, and slight to moderate depletions in HREE compared to average N-MORB composition as well as the MORB-type lavas from the Phoenix and Pacific–Antarctic Ridges (Fig. 5a). Their MORB-normalized patterns are similar to those of the West Antarctic rift basalts. Unlike the Bransfield Strait axial lavas with typical BABB trace element distributions, they exhibit no negative HFSE anomalies. The negative slopes in MORB-normalized patterns indicate stronger enrichments in more incompatible elements than less incompatible ones. The samples all display strong positive anomalies of Pb and Sr and slight negative anomalies of Y on normalized plots (Fig. 5a). On a CI-chondrite-normalized diagram, the rocks show sub-parallel patterns characterized by enrichments in all REE relative to chondrite (Fig. 5b). Steep negative slopes in chondrite-normalized profiles indicate an increasing degree of enrichment in REE in order of increasing incompatibility, a feature commonly observed in OIB-type intraplate lavas worldwide (e.g. Sun & McDonough, 1989).

Sr, Nd, Hf and Pb isotopes

Radiogenic isotope ratios of the samples are listed in Table 1. The volcanic rocks are the products of young (6 to <1 Ma) magmatic activity with insignificant in-situ radiogenic ingrowth since eruption, such that the isotopic ratios of the rocks represent their source composition. The samples show low $^{87}Sr/^{86}Sr$ (0.70301–0.70365), accompanied by high $^{143}Nd/^{144}Nd$ (0.51283–0.51294) and $^{176}Hf/^{177}Hf$ (0.28291–0.28298) ratios. Their lead isotope ratios also vary within a limited range with $^{206}Pb/^{204}Pb$, $^{207}Pb/^{204}Pb$, $^{208}Pb/^{204}Pb$ ratios of 18.797–18.953, 15.577–15.634, and 38.414–38.701, respectively.

On a $^{143}Nd/^{144}Nd$ vs. $^{87}Sr/^{86}Sr$ diagram, the samples cluster in the depleted quadrant of the mantle array compared to Bulk Silicate Earth (BSE; Hart *et al.*, 1992). They scatter between the BSE and MORB fields, although they plot closer to MORB-like compositions (Fig. 6a). With their relatively low $^{143}Nd/^{144}Nd$ ratios, the samples mostly fall slightly below the mantle array. They have lower $^{87}Sr/^{86}Sr$ and higher $^{143}Nd/^{144}Nd$ ratios than the South Shetland Islands arc lavas (Machado *et al.*, 2005; Haase *et al.*, 2012), and higher $^{87}Sr/^{86}Sr$ and lower $^{143}Nd/^{144}Nd$ ratios than the Phoenix Ridge and Shackleton Fracture Zone lavas (Haase *et al.*, 2011) (Fig. 6a). They resemble the Cenozoic intraplate alkaline volcanic rocks from the West Antarctic rift system (Aviado *et al.*, 2015; Panter *et al.*, 2018) but have relatively lower $^{143}Nd/^{144}Nd$ ratios than the subalkaline lavas from the Bransfield Strait (Keller *et al.*, 2002; Fretzdorff *et al.*, 2004) at a given $^{87}Sr/^{86}Sr$ (Fig. 6a).

$^{206}Pb/^{204}Pb$ and $^{208}Pb/^{204}Pb$ ratios of the alkaline lavas are generally higher than the MORB lavas from the Pacific–Antarctic Ridge, but distinctly lower than the Cenozoic mafic alkaline OIB-type intraplate lavas of the West Antarctic rift (Fig. 6). Unlike the lavas

Table 1: Sr–Nd–Hf–Pb isotope data for the alkaline volcanic rock samples from the James Ross Island Volcanic Group

Sample name	$^{87}Sr/^{86}Sr$	$\sigma/\sqrt{n}$	$^{143}Nd/^{144}Nd$	$\sigma/\sqrt{n}$	εNd	$^{176}Hf/^{177}Hf$	$\sigma/\sqrt{n}$	εHf	$^{208}Pb/^{204}Pb$	$\sigma/\sqrt{n}$	$^{207}Pb/^{204}Pb$	$\sigma/\sqrt{n}$	$^{206}Pb/^{204}Pb$	$\sigma/\sqrt{n}$	$\Delta^{8/4}$	$\Delta^{7/4}$
C-4	0.703415	0.000010	0.512860	0.000004	4.22	0.282935	0.000004	5.78	38.6070	0.0011	15.6343	0.0004	18.7974	0.0005	25.40	10.57
JR-12	0.703373	0.000010	0.512880	0.000005	4.60	0.282956	0.000006	6.51	38.6580	0.0013	15.6153	0.0005	18.9182	0.0005	15.89	7.36
JR-32	0.703442	0.000010	0.512870	0.000004	4.40	0.282920	0.000006	5.22	38.6140	0.0013	15.6347	0.0004	18.8094	0.0005	24.65	10.48
JR-74	0.703132	0.000013	0.512939	0.000004	5.76	0.282948	0.000005	6.22	38.5496	0.0017	15.6042	0.0006	18.9249	0.0008	4.24	6.17
JR-88A	0.703288	0.000010	0.512890	0.000004	4.80	0.282945	0.000007	6.11	38.7019	0.0012	15.6226	0.0004	18.9532	0.0006	16.05	7.70
JR-104	0.703074	0.000011	0.512949	0.000005	5.96	0.282969	0.000006	6.97	38.5095	0.0011	15.5921	0.0004	18.8944	0.0004	3.91	5.29
JR-109	0.703016	0.000009	0.512949	0.000004	5.96	0.282967	0.000007	6.88	38.4911	0.0013	15.5882	0.0005	18.9038	0.0006	0.94	4.81
JR-113	0.703664	0.000013	0.512844	0.000003	3.89	0.282912	0.000007	4.94	38.6790	0.0012	15.6299	0.0005	18.8792	0.0006	22.70	9.24
JR-116	0.703035	0.000011	0.512942	0.000004	5.82	0.282962	0.000007	6.73	38.5498	0.0012	15.6041	0.0005	18.9201	0.0005	4.85	6.21
JR-126	0.703056	0.000014	0.512945	0.000004	5.89	0.282982	0.000005	7.42	38.5056	0.0014	15.5912	0.0005	18.9084	0.0006	1.84	5.05
TA-1	0.703433	0.000010	0.512870	0.000005	4.42	0.282935	0.000008	5.76	38.6736	0.0013	15.6246	0.0005	18.9083	0.0005	18.65	8.39
TA-3	0.703443	0.000012	0.512873	0.000004	4.46	0.282929	0.000006	5.54	38.6801	0.0015	15.6270	0.0005	18.9052	0.0005	19.67	8.67
VG-1	0.703226	0.000011	0.512906	0.000004	5.13	0.282965	0.000006	6.83	38.6216	0.0012	15.6221	0.0004	18.8814	0.0005	16.70	8.44
VG-3	0.703211	0.000015	0.512905	0.000004	5.11	0.282968	0.000006	6.94	38.6368	0.0011	15.6240	0.0004	18.8922	0.0005	16.92	8.51
VG-8	0.703557	0.000013	0.512869	0.000004	4.41	0.282930	0.000007	5.57	38.6014	0.0013	15.6186	0.0005	18.8308	0.0006	20.80	8.63
EG-1	0.703028	0.000011	0.512939	0.000005	5.76	0.282954	0.000005	6.44	38.4148	0.0014	15.5775	0.0006	18.8321	0.0005	1.98	4.51
EG-3	0.703423	0.000012	0.512886	0.000005	4.73	0.282941	0.000006	5.96	38.6114	0.0015	15.6080	0.0005	18.8892	0.0005	14.74	6.94
EG-5	0.703432	0.000012	0.512886	0.000005	4.73	0.282940	0.000007	5.94	38.6133	0.0016	15.6085	0.0006	18.8878	0.0007	15.10	7.01

εNd and εHf are reported relative to the chondritic values of 0.512638 and 0.282772, respectively. $\Delta^{8/4}$ and $\Delta^{7/4}$ are indices of ^{208}Pb and ^{207}Pb enrichment relative to the NHRL values. Errors quoted are the internal precision at 2SD.

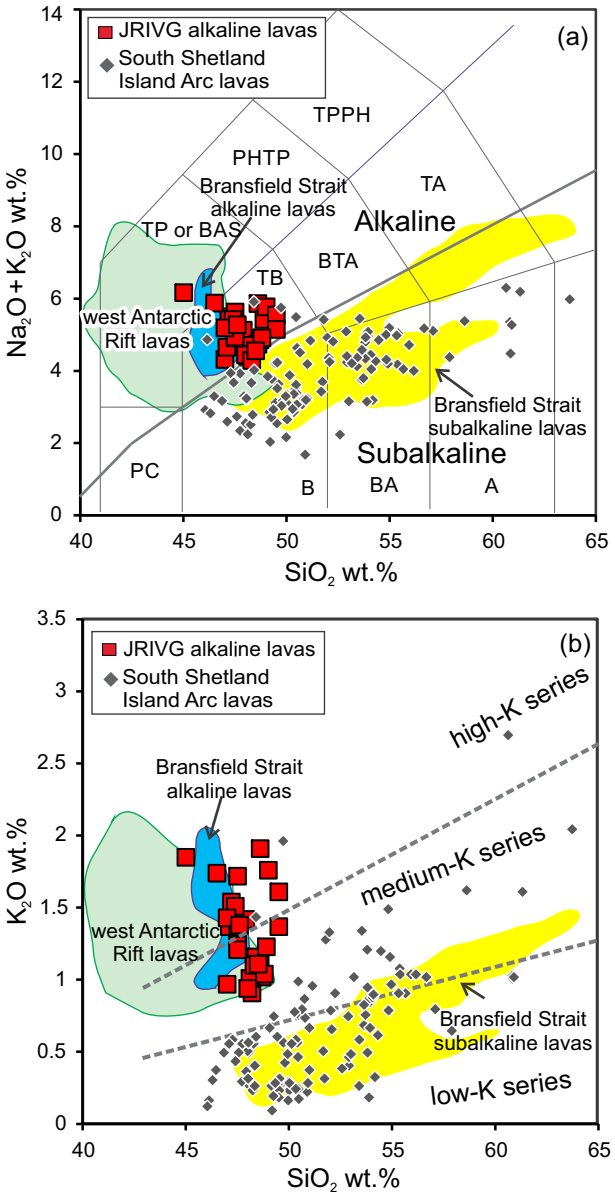

Fig. 4. a-b- Classification of the JRIVG lavas on a total alkali vs. silica diagram of Le Bas *et al.* (1986), and a K_2O vs. SiO_2 diagram of Peccerillo & Taylor (1976). Also plotted for comparison are the lava compositions from the South Shetland Island Arc (Machado *et al.*, 2005; Haase *et al.*, 2012), the Bransfield Strait (Keller *et al.*, 2002; Fretzdorff *et al.*, 2004 ; Haase *et al.*, 2011) and the West Antarctic Rift System (Aviado *et al.*, 2015; Panter *et al.*, 2018). *Key to abbreviations:* PC: picrobasalt; B: basalt; BA: basaltic andesite; A: andesite; TB: trachybasalt; BTA: basaltic trachyandesite; TA: trachyandesite; T: trachyte; TD: trachydacite; BS: basanite; TP: tephrite; TPPH: tephriphonolite; PHTP: phonotephrite; PH: phonolite.

of the West Antarctic rift, the samples show no contribution from a HIMU-type component with highly radiogenic Pb isotope signatures. Lead isotope variations of the lavas exhibit some similarities to those of the older volcanic suite of the South Shetland island arc and young lavas from the axial eruption centers along the Bransfield Basin, although they cluster within a relatively limited compositional range (Fig. 6c). With their $\Delta^{7/4}$ and $\Delta^{8/4}$ values of up to 10.57 and 25.40, respectively, they show variable enrichments in $^{207}Pb/^{204}Pb$ and $^{208}Pb/^{204}Pb$ ratios for a given $^{206}Pb/^{204}Pb$ relative to the northern hemisphere reference line (NHRL; $\Delta^{7/4}$ and $\Delta^{8/4}$ are indices of ^{207}Pb and ^{208}Pb enrichment relative to the NHRL values, respectively; Hart, 1984) (Table 1; Fig. 6b-c).

PETROGENESIS

Effects of post melting magmatic processes

Mantle-derived basaltic magmas that assimilate continental crustal rocks would be expected to have high $^{87}Sr/^{86}Sr$ and $^{207}Pb/^{204}Pb$ ratios coupled with low $^{143}Nd/^{144}Nd$ and $^{176}Hf/^{177}Hf$ ratios, as well as high relative abundances of LILE. Compositional variations of the studied alkaline lavas suggest no significant effects of continental crustal contamination. Specifically, the lavas have unfractionated LILE/HFSE ratios which lack negative HFSE anomalies (Fig. 5a). The coherent behavior of highly incompatible elements (e.g. Th and Ta), as displayed by OIB-like trace element patterns of the samples, also suggest that the rocks are free of the effects of crustal contamination for which elevated LILE/HFSE ratios would be expected. The lack of any clear variation between silica and K_2O contents of the lavas provides further constraints against compositional modification through input of continental crust (Fig. 4b).

However, a large range of major and trace element abundances for relatively limited change in radiogenic isotope ratios indicates variable effects of fractional crystallization as the major differentiation process. Variations of compatible trace element (Cr and Ni) and Fe_2O_3 concentrations with MgO contents suggest that the magmas have undergone variable extents of low-pressure fractional crystallization of olivine (Fig. 7). This is consistent with the observations from petrographic analyses which indicate the predominance of olivine separation during magmatic differentiation. The primary magma compositions calculated using the PRIMELT algorithm of Herzberg & Asimow (2015) also suggest that the lavas were formed by ~18–40% olivine fractionation, which caused a systematic decrease in Mg and Ni contents of the primary melts (Fig. 7). The estimated primary melt compositions, recalculated using the olivine control line and by redissolving olivine to attain chemical equilibrium between olivine and the corresponding melts, have MgO contents of ~16 to 20 wt.% with Ni concentrations of 330 to 390 $\mu g/g$ (Fig. 7).

Mantle source characteristics

Figure 8 presents the compositional variations of magmatic rocks in the region between the Antarctic–Phoenix Ridge and the Antarctic Peninsula. Also plotted for comparison are the Cenozoic intraplate alkaline lavas of the West Antarctic rift system (Aviado *et al.*, 2015; Panter *et al.*, 2018) and the lavas of the East Scotia Ridge (Pearce *et al.*, 1995). The young lavas (< 7 Ma) in the back-arc region behind the South Shetland islands arc display a wide variety of geochemical signatures, reflecting considerable source compositional heterogeneities on small length scales. Along-axis variations in basalt chemistry within the Bransfield Strait reveal melt derivation from isotopically depleted, MORB-source-like mantle with trace element relative abundances indicative of a highly variable subduction component (Keller *et al.*, 1992; Hole *et al.*, 1995; Fretzdorff *et al.*, 2004). Further south-eastward from the rift axis to the northern Antarctic Peninsula, the lava chemistry becomes dominated by intraplate varieties. This implies that the supra-slab mantle is highly heterogeneous, reflecting the effects of different slab-derived components.

The effects of subduction-induced element transport on the chemical characteristics of mantle wedge peridotites are examined here first by approximating the regional upper mantle composition prior to any subduction input. Geochemical variations of

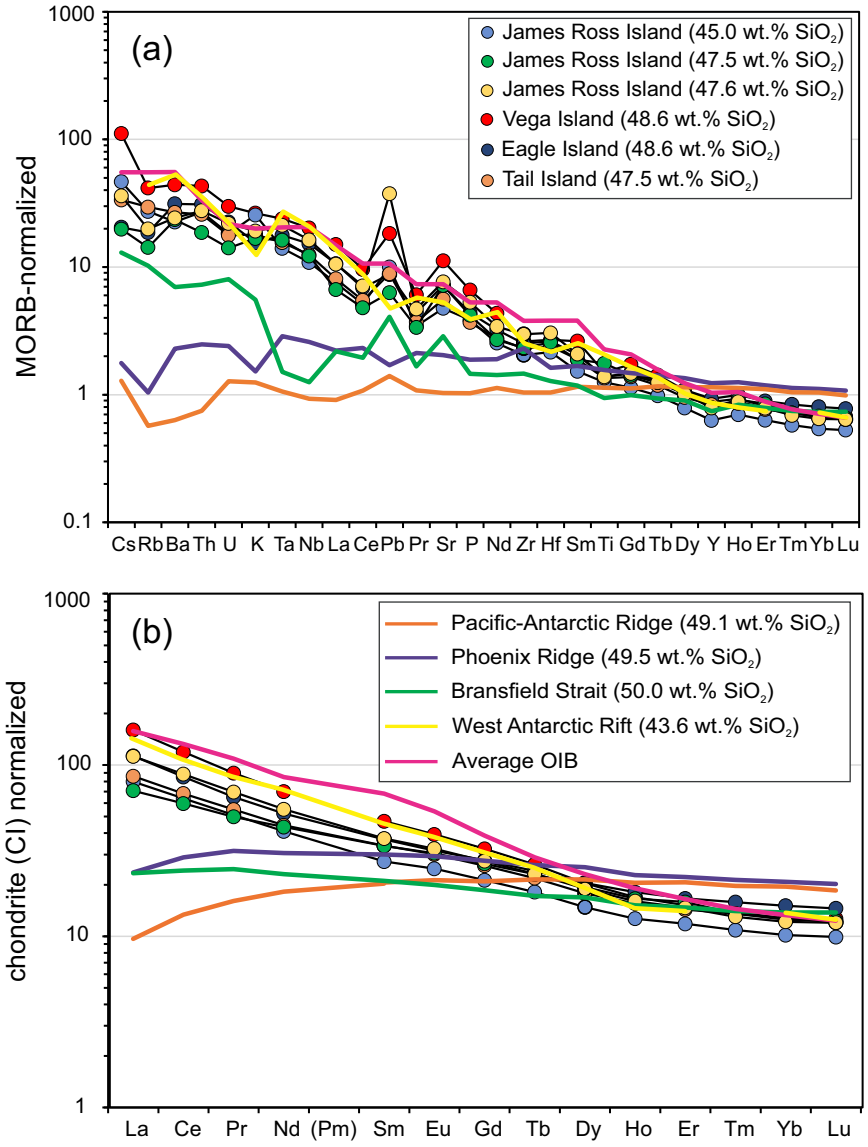

Fig. 5. a- N-MORB and **b-** Chondrite-normalized trace element patterns for the JRIVG lavas. The average OIB (Sun & McDonough, 1989), and the basaltic lava compositions with similar SiO_2 contents from the Pacific–Antarctic Ridge (Hamelin *et al.*, 2011), the Phoenix Ridge (Haase *et al.*, 2011) and the Bransfield Strait (Keller *et al.*, 2002) are plotted for comparison. N-MORB and Chondrite normalizing values are from Sun & McDonough (1989) and Boynton (1984), respectively.

the lavas from the Antarctic–Phoenix Ridge and the Shackleton Fracture Zone can be used to determine the upper mantle composition. Lavas from these sites range in composition from N-MORB to E-MORB (Haase *et al.*, 2011), indicating that the local shallow convective mantle is similar in composition to typical Depleted MORB Mantle with some small-scale enrichments that gave rise to the E-MORB varieties. On a plot of $^{207}Pb/^{204}Pb$ vs. $^{206}Pb/^{204}Pb$ (Fig. 8a), the positive linear trend defined by the compositions of these MORB lavas from the unmodified sources therefore likely represents the local mantle array, which also corresponds to the regional mantle trend defined as the SW Indian Ridge – South American-Antarctic Ridge (SWIR – SAAR) array with the depleted and enriched endmembers represented by typical N-MORB and the lavas of the Bouvet Triple Junction, respectively (Pearce *et al.*, 1995).

Displacements from this mantle array to higher $^{207}Pb/^{204}Pb$ likely reflect involvement of a subduction component with relatively more radiogenic $^{207}Pb/^{204}Pb$, while elevated $^{206}Pb/^{204}Pb$ ratios relative to the mantle array should imply variable involvement of a HIMU component (Fig. 8a). The vertical trend in $^{207}Pb/^{204}Pb$ vs. $^{206}Pb/^{204}Pb$ isotope space should therefore be associated with a slab-derived component in the genesis of alkaline lavas. This is also consistent with the findings of Altunkaynak *et al.* (2019) where trace element variations and low Ca contents of olivine phenocrysts from the same lava suites were interpreted to suggest that the alkaline magmas were derived from an H_2O-rich parental melt generated by partial melting of a hydrated peridotite.

As shown in Fig. 8a, the lava compositions from much of the back-arc region behind the South Shetland Arc are displaced from the diagonal mantle array to higher $^{207}Pb/^{204}Pb$ which likely reflects the effects of slab-derived components. Subducted slab involvement is also shown by the increase in $^{87}Sr/^{86}Sr$, Th/La and Pb/Pb* (Pb* is taken as extrapolated Pb calculated using N-MORB normalized concentrations of Ce, Pb and Pr) with respect to the ambient mantle composition in Fig. 8. Sharp increases in $^{87}Sr/^{86}Sr$,

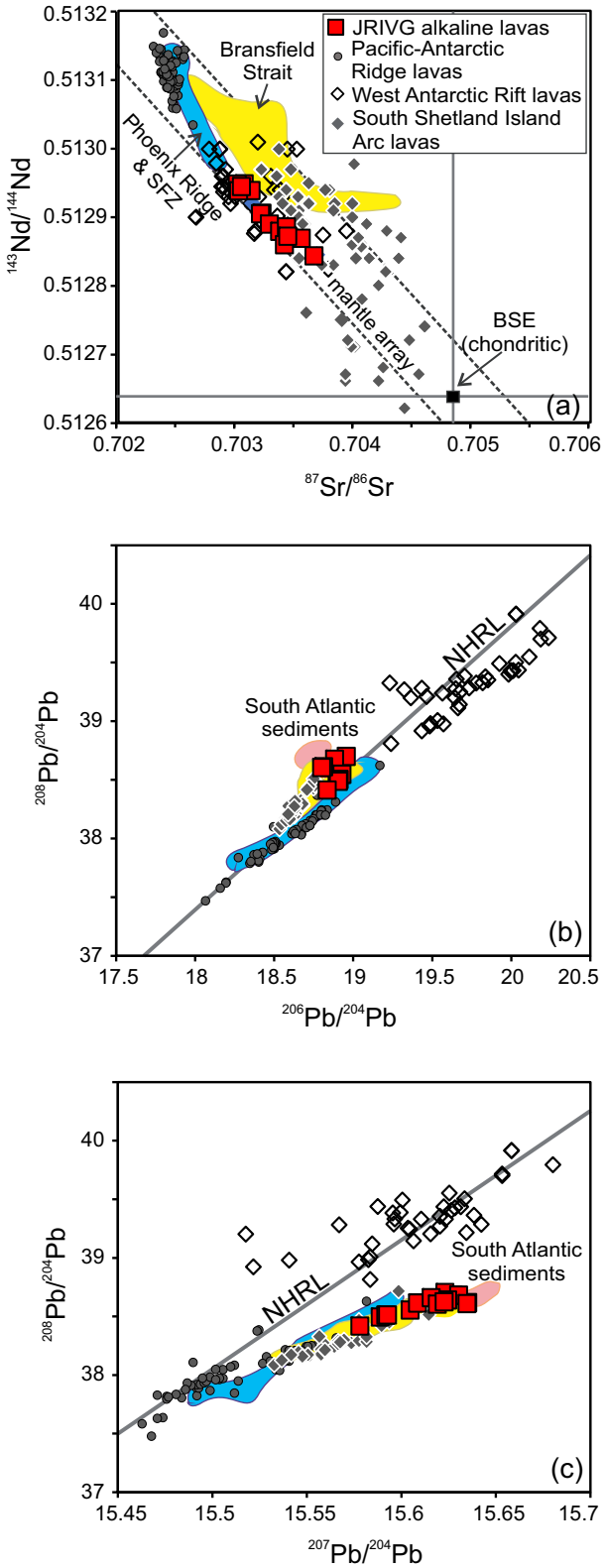

Fig. 6. a- $^{143}Nd/^{144}Nd$ vs. $^{87}Sr/^{86}Sr$; **b-** $^{208}Pb/^{204}Pb$ vs. $^{206}Pb/^{204}Pb$; and **c-** $^{208}Pb/^{204}Pb$ vs. $^{207}Pb/^{204}Pb$ plots showing the isotopic variation for the JRIVG lavas. The data plotted for comparison are from the basaltic lavas from the Pacific–Antarctic Ridge (Hamelin *et al.*, 2011), Phoenix Ridge and Shackleton Fracture Zone (Haase *et al.*, 2011), the Bransfield Strait (Keller *et al.*, 2002; Fretzdorff *et al.*, 2004; Haase *et al.*, 2011), the South Shetland Islands Arc (Machado *et al.*, 2005; Haase *et al.*, 2012) and the West Antarctic Rift System (Aviado *et al.*, 2015; Panter *et al.*, 2018).

Th/La and Pb/Pb* ratios form vertical trends that diverge from the regional mantle array toward the compositional field of the South Atlantic sediments (Barry *et al.*, 2006). The variations in Fig. 8 further show that, although the slab melt/fluid contribution is observed in almost all the lava compositions from the back-arc region, its effect is less pronounced for the alkaline lavas in comparison with the Bransfield Basin lavas.

Slab-derived components may be introduced into the mantle via aqueous fluids released from the slab at temperatures below the wet solidus of crustal rocks, or by interaction of wedge peridotites with hydrous slab melts generated at higher temperatures (Prouteau *et al.*, 2001; Mibe *et al.*, 2011; Spandler & Pirard, 2013). The former is known to enrich the overlying mantle in fluid-mobile trace elements, while the latter generally results in enhancements in all highly incompatible elements that are partitioned preferentially into the melt during slab melting.

The possible effects of slab-derived fluids and melts for the alkaline suite are illustrated on a plot of Th/Yb vs. Ta/Yb (Pearce, 1983) in Fig. 9a, where lava compositions from the entire back-arc region are also plotted. Two different trends diverge from the depleted MORB source-like composition, indicating that slab contribution affects the supra-slab mantle region in two different ways. One is the diagonal MORB – OIB array with a slope close to unity, while the other is defined by increasing Ta/Yb with a larger increase in Th/Yb, indicating a more extreme enrichment in Th than Ta (Fig. 9a). A similar effect is also observed in Th/Nb vs. $^{206}Pb/^{204}Pb$ variations (Fig. 9b), where the alkaline rocks lie within the mantle array, while the lavas from the Bransfield Strait and the South Shetland arc exhibit greater Th/Nb ratios at a given $^{206}Pb/^{204}Pb$.

The variations in isotope and trace element systematics presented in Fig. 8 and 9, therefore, indicate that the slab components generated at different depths may differ in terms of relative abundances of LILE and HFSE, even though their effects on isotopic variations may be similar. In comparison with the Bransfield Strait axial lavas, which display enrichments in fluid mobile elements with higher Th/Ta than the MORB-OIB trend, the alkaline lavas all have MORB-like Th/Ta ratios exhibiting no selective enrichments of fluid-soluble elements (Fig. 9). The variations shown in Fig. 8 and 9, therefore, likely reflect slab melt rather than aqueous fluid involvement for the alkaline melts.

Nature of the slab melt component

Experimental petrological studies suggest that dry peridotite mantle rocks are unlikely to be the source of alkali-rich intraplate basaltic magmas (Hirose & Kushiro, 1993). Generation of basaltic melts with lower silica and aluminum, and higher calcium and alkali contents than that produced by partial melting of dry lherzolite is generally explained by the interaction of mantle peridotites with eclogite-derived slab melts (Sajona *et al.*, 1996; Yaxley & Green, 1998; Mallik & Dasgupta, 2013; Rosenthal *et al.*, 2014). Slab components may be either carbonate melt or silicate melt with or without carbonatite components, depending on the type of material incorporated into the mantle (Dai *et al.*, 2017).

Carbonate melt metasomatism is a commonly suggested mechanism in the petrogenesis of silica-deficient alkali-rich intraplate basaltic magmas in general (Hirose, 1997). However, several lines of evidence suggest that this is an unlikely explanation in genesis of the alkaline lavas here. The alkaline lavas appear to have higher silica and lower total alkali contents than experimentally determined values for carbonated lherzolite-derived melts (e.g. Mallik & Dasgupta, 2013). In addition, basaltic melts generated by melting of carbonated peridotite are typically

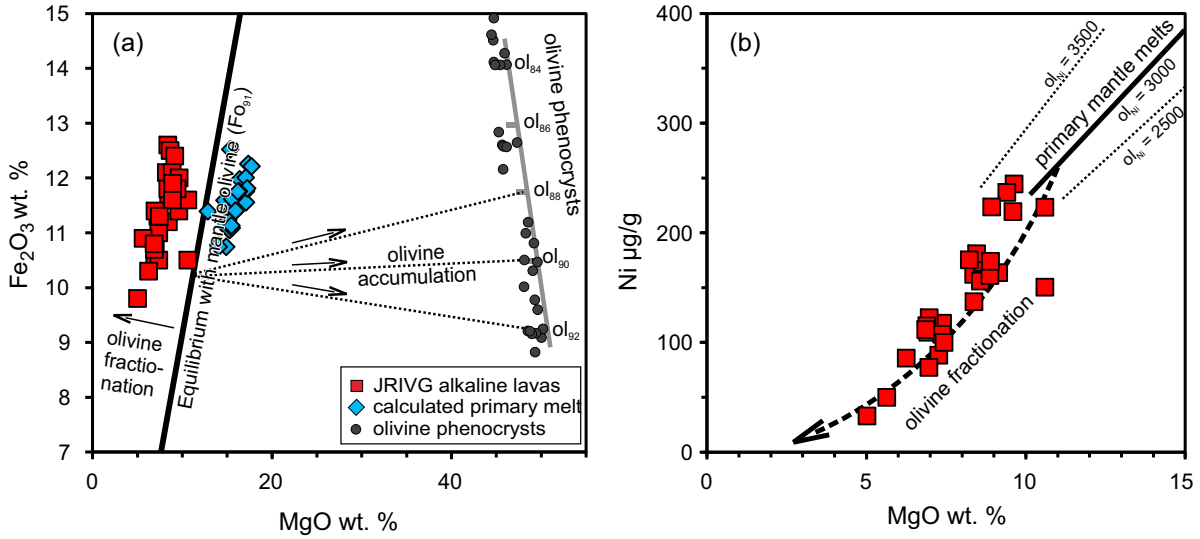

Fig. 7. a- Fe_2O_3 vs. MgO variations of the alkaline lavas reflecting the effects of olivine fractionation on primary melt compositions. The heavy line represents the primary melt composition calculated using a Fe/Mg olivine/melt partition coefficient of 0.3 assuming a Fe_2O_3/MgO ratio of 0.9 for the melt that is in equilibrium with mantle olivine (Fo_{91}) (e.g. Aldanmaz *et al.*, 2006). Olivine Fo contents that are used to identify the olivine control line are from the data presented in Altunkaynak *et al.* (2019). **b-** Ni vs. MgO variations of the alkaline lavas showing the degree of olivine fractionation. The solid lines represent primary melt compositions in equilibrium with olivine with different Ni abundances.

characterized by very high concentrations of LREE (as high as ~1000 times greater than chondritic values), the presence of negative Ti anomalies, and highly fractionated Zr/Hf of up to 100 (e.g. Bizimis *et al.*, 2003). All these characteristics are in contrast with the limited LREE enrichment (<100 × CI chondrite), the absence of negative Ti anomalies and the lower Zr/Hf (30–37) of the alkaline rocks.

Furthermore, unlike reactions with silicate melt during which dissolution of olivine and precipitation of orthopyroxene forms olivine-poor mantle lithologies, carbonatite metasomatism is suggested to preferentially dissolve orthopyroxene, generating olivine- and clinopyroxene-rich reaction products (Gervasoni *et al.*, 2017). Melt generation from carbonatite-metasomatized peridotite would therefore be dominated by incongruent melting of clinopyroxene which would produce melts with high CaO/Al_2O_3 (> 1) ratios (e.g. Mallik & Dasgupta, 2013). The relatively lower (< 0.6) CaO/Al_2O_3 ratios of the alkaline magmas here are in contrast with the melting of carbonated peridotite (supplementary Table 1). The presence of olivine phenocrysts with lower Mn/Fe and Ca/Fe ratios in the alkaline lavas (Altunkaynak *et al.*, 2019) provides further constraints against melt generation from olivine- and clinopyroxene-rich sources and hence carbonate-rich melt metasomatism. It is thus reasonable to infer that the mantle source from which the alkaline lavas were derived has been affected by silicate melt metasomatism.

Effects of melt metasomatism on the source trace element composition

As shown above, the isotopic and trace element variations of the alkaline rocks suggest melt generation from a peridotite source metasomatized by slab melts. Slab-derived hydrous melts may be produced in relatively warm subduction zones via advection of metamorphic fluids through the uppermost crustal part of the slab (Walowski *et al.*, 2016). Previous studies have shown that melting of fluid-saturated eclogites will result in consumption of clinopyroxene to a large extent, producing siliceous melt rich in incompatible elements and saturated with clinopyroxene and garnet (Ringwood, 1990; Yaxley & Green, 1998). On their ascent, these melts extensively react with the surrounding peridotite, transforming the variably depleted wedge peridotites into garnet lherzolite or refertilized harzburgite which likely also contains hydrous phases (Sekine & Wyllie, 1982; Gervasoni *et al.*, 2017).

Dissolution of olivine during the reaction of wedge peridotites with a volatile-rich slab melt has been previously shown to cause precipitation of new phases including Fe-rich orthopyroxene, Na-rich clinopyroxene, garnet, and amphibole (Na-richterite) (Rapp *et al.*, 1999; Prouteau *et al.*, 2001). Although amphibole formation is a ubiquitous feature in almost all subduction settings, its effects in terms of the compositions of newly formed metasomatic assemblages may differ significantly depending on the rate of melt influx and the composition of the slab melt component (Rapp *et al.*, 1999; Corgne *et al.*, 2018). The presence of compositionally different metasomatic amphiboles in many mantle xenolith suites worldwide indicates that reactions with compositionally diverse slab melts and fluids may have distinct metasomatic signatures (Coltorti *et al.*, 2007). At sub-arc depths, such reactions likely produce metasomatic amphiboles with relative depletions of HFSE, which is mainly the result of retention of Ti, Nb and Ta in residual rutile or amphibole during slab dehydration, while at higher pressures, dissolution of rutile results in elevated HFSE concentrations in metasomatizing melts, leading to precipitation of HFSE-enriched amphibole (Coltorti *et al.*, 2007).

We have attempted here to identify semi-quantitatively the trace element composition of the mantle source by applying the incongruent dynamic melting inversion method described in Zou & Reid (2001). The modeling was applied using the fractionation corrected trace element compositions of cogenetic lavas. To estimate the parental melt compositions, the fractionation signature was inverted by adding the liquidus olivine back into the melt using the approach of Herzberg & Asimow (2015). Trace element concentrations of the corresponding primary melts were then estimated using mineral/melt partition coefficients given in Bédard (2005).

Considering the effects of interaction with slab-derived hydrous melts in modifying the composition of the mantle wedge, the source trace element composition was modeled for

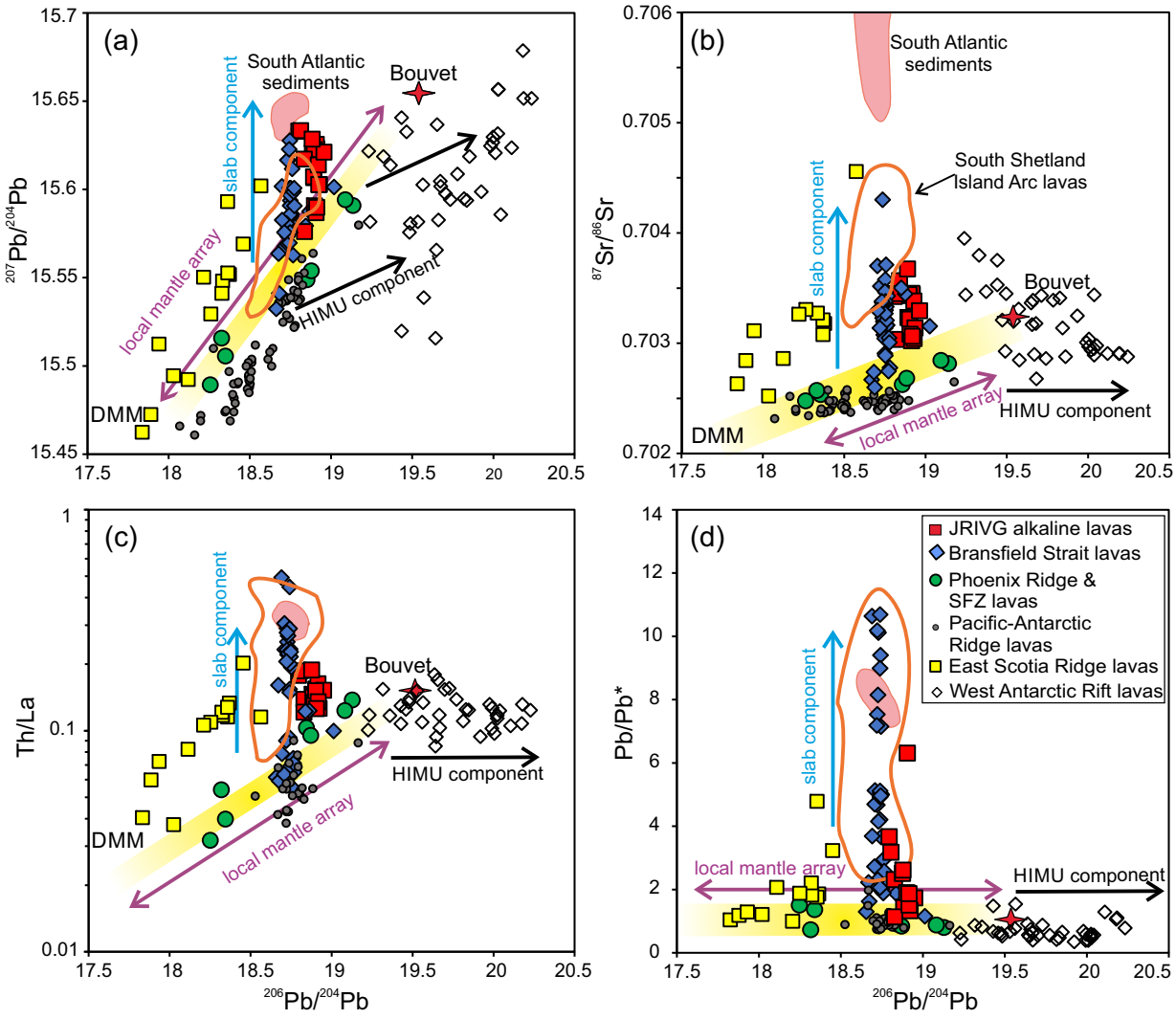

Fig. 8. a- $^{207}Pb/^{204}Pb$; **b-** $^{87}Sr/^{86}Sr$; **c-** Th/La; and **d-** Pb/Pb∗ variations with $^{206}Pb/^{204}Pb$ for the JRIVG lavas are compared with the young (< 7 Ma) lavas erupted along the Pacific–Antarctic Ridge, Phoenix Ridge, Shackleton Fracture Zone (SFZ), the Bransfield Strait, the East Scotia Ridge, as well as the Cenozoic intra-plate type alkaline lavas of the West Antarctic Rift System to show the regionwide mantle compositional heterogeneities. The data sources for basaltic lavas used for comparison are as in Fig. 6. The compositions of the East Scotia Ridge and the Bouvet Triple Junction lavas are based on the data presented in Pearce *et al.* (1995).

the alkaline lavas assuming an amphibole-bearing source with modal mineralogy estimated using the compositions of melt-metasomatized mantle xenoliths from southernmost South America (e.g. Wang *et al.*, 2007). The modeled source of the alkaline melts reveals significant enrichments in almost all highly incompatible elements compared to the local depleted mantle, the composition of which was estimated to be similar to a typical depleted MORB source by employing anhydrous lherzolite melting using the Phoenix Ridge lava data (Fig. 10).

Incompatible trace element enrichments are particularly obvious for all LILE, HFSE and LREE, while M-HREE contents may be slightly more depleted than the local depleted mantle depending on the source mantle being either spinel- or garnet-lherzolite. The calculated source composition has elevated concentrations of Ta, Nb and Ti with respect to the neighboring elements with similar incompatibilities (Fig. 10). Comparison with the calculated source of the Bransfield Strait lavas indicates that the modeled source of the alkaline melts is enriched in all highly incompatible elements except for the HREE. The enrichment is particularly obvious for Nb and Ta, for which the source of the Bransfield lavas displays prominent negative anomalies associated with fluid-mobile LILE enrichments.

Subduction-driven enrichment of the back-arc mantle

Slab-derived siliceous melts may be produced by fluid-assisted partial melting of basaltic oceanic crust and overlying sediments during warm slab subduction (Prouteau *et al.*, 2001; Mibe *et al.*, 2011; Walowski *et al.*, 2016). Subducted sediments generally have high Th/La ratios and low $^{143}Nd/^{144}Nd$ and $^{176}Hf/^{177}Hf$ (Plank, 2005; Chauvel *et al.*, 2008). Sediment-derived melt involvement should therefore result in an increase in Th/La and a decrease in Nd and Hf isotope ratios. The basaltic oceanic crust, on the other hand, is characterized by lower Th/La and MORB-like Nd and Hf isotope ratios. As shown in Fig. 8, the alkaline lavas investigated here have significantly lower Th/La ratios (<0.02) compared to the South Atlantic ocean-floor sediments (Barry *et al.*, 2006), and Th/La ratios increase only slightly with increasing $^{207}Pb/^{204}Pb$. This, along with the relatively high $^{143}Nd/^{144}Nd$ and $^{176}Hf/^{177}Hf$ ratios of the samples, suggests that sediment-derived

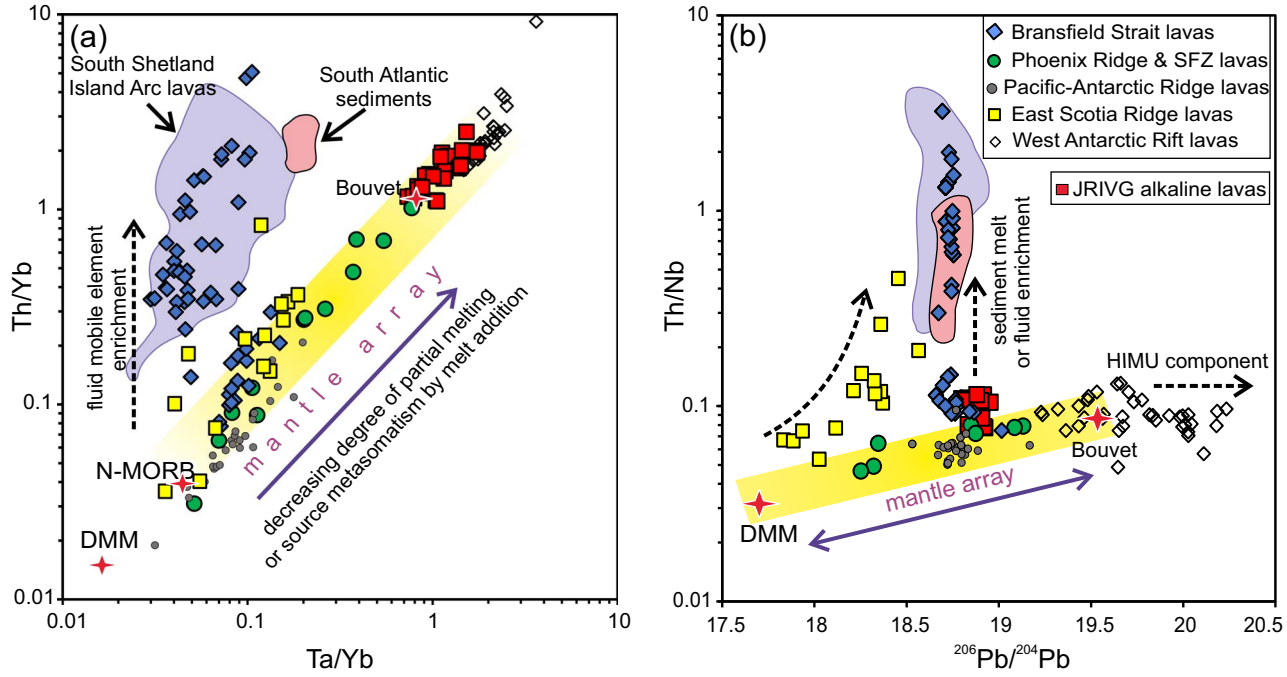

Fig. 9. a- Th/Yb vs. Ta/Yb; and **b-** Th/Nb vs. $^{206}Pb/^{204}Pb$ diagrams showing the regionwide variations in melt chemistry using the lava compositions presented in Fig. 8. Two distinct trends in (a) reflect the variable effects of subduction enrichment through slab dehydration and slab melt contribution in the genesis of mantle derived magmas.

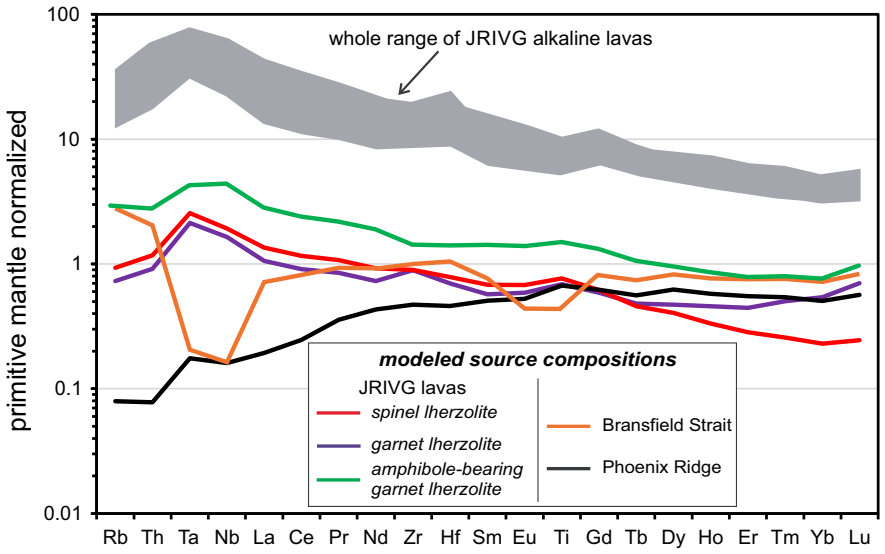

Fig. 10. Primitive mantle-normalized incompatible trace element patterns showing the likely mantle source compositions calculated by dynamic melting inversion (DMI) method using the data from the JRIVG lavas with the parameters described in Zou & Reid (2001). The modelling utilizes the enrichment ratios of two different incompatible elements for two samples that are assumed to have originated from the same source by different degrees of partial melting. The source compositions for the JRIVG lavas were calculated for both anhydrous (with source modal mineralogy of $ol_{0.578} + opx_{0.270} + cpx_{0.119} + sp_{0.033}$ and $ol_{0.597} + opx_{0.211} + cpx_{0.076} + gt_{0.030}$ for spinel and garnet lherzolite, respectively) and amphibole-bearing peridotite (with source modal mineralogy of $ol_{0.563} + opx_{0.226} + cpx_{0.046} + gt_{0.115} + amp_{0.050}$). Modelling with anhydrous and hydrous peridotite melting reveal ~3 to 12 and ~6 to 18% of partial melting, respectively. Also shown for comparison are the source compositions calculated using the compositions of the axial lavas from the Phoenix Ridge and the Bransfield Basin using the published data from the mafic lava compositions (Fretzdorff *et al.*, 2004; Haase *et al.*, 2011) and assuming partial melting in the spinel stability zone.

melts are unlikely to be the only slab component responsible for the enriched isotopic and trace element signatures of the alkaline lavas.

In general, MORB basalts have lower Lu/Hf than their source and this will result in time-integrated decoupling of Hf from Nd isotope ratios (Chauvel *et al.*, 2008). Thus, a basaltic crust that undergoes partial melting will produce melts with $^{176}Hf/^{177}Hf$ and $^{143}Nd/^{144}Nd$ ratios plotting below the diagonal mantle array, while ocean floor sediments generally have higher $^{176}Hf/^{177}Hf$ and plot above or to the far left of the mantle array (Fig. 11a). Decoupling between Hf and Nd isotope ratios and increase in $^{176}Hf/^{177}Hf$ isotopes at a given $^{143}Nd/^{144}Nd$ is particularly common for zircon-deficient pelagic sediments that usually have lower Hf/Nd and higher Lu/Hf ratios and develop more radiogenic Hf,

while zircon-bearing continental crust-derived sediments possess lower $^{176}Hf/^{177}Hf$ ratios (Chauvel *et al.*, 2008). As shown in Fig. 11a, the alkaline lavas plot slightly below the mantle array and form a compositional trend reflecting the effect of altered basaltic crust with a variable contribution from mixed sources of pelagic and volcanogenic sediments. It is therefore more reasonable to infer the involvement of a composite slab melt containing both basaltic crust and sediment-derived melt. This is also evident from the negative correlation of $^{176}Hf/^{177}Hf$ with Lu/Hf (Fig. 11b) which requires the involvement of a component having higher $^{176}Hf/^{177}Hf$ and lower Lu/Hf than the local mantle source and is likely explained by eclogite melting with garnet residue.

Isotopic evidence indicating slab melt involvement in mantle source hybridization is also supported by trace element variations of the lavas which provide further constraints on mineral compositional variations and melting conditions of slab material. The alkaline lavas all display Pb enrichments with respect to the neighboring elements in multi-element plots (Fig. 5a). Positive Pb spikes are common in arc and back-arc magmas, and with no significant effect of contamination by continental crust, such anomalies are interpreted to reflect selective enrichment by slab fluid influx or sediment melt addition. When coupled with negative HFSE anomalies, such positive Pb spikes are interpreted to reflect the relatively immobile character of HFSE in subduction fluids. In the absence of HFSE depletions, as is the case for the alkaline lavas here, Pb enrichment likely reflects the distinct trace element behavior during slab dehydration/melting at different depths rather than being the result of greater mobility of LILE.

A similar positive spike in multi-element plots is observed in Sr, but not in other LILEs (Fig. 5a). Such a distinct fluid-mobile element behavior is probably the result of Pb-Sr and LILEs partitioned preferentially into different hydrous minerals in the subducted slab. Epidote group minerals (e.g. epidote, zoisite and allanite) retain Pb and Sr along with Th, U and REE to a great extent, while phengite and lawsonite are the major hosts of other LILEs (Spandler *et al.*, 2003; Xiao *et al.*, 2012; Spandler & Pirard, 2013). Slab dehydration at sub-arc depths is mainly related to the progressive breakdown of hydrous minerals (Schmidt & Poli, 1998). This releases large volumes of water and removes a significant amount of LILEs from the slab, while some portions of Pb and Sr are retained in the residue and held mainly by epidote/zoisite (Xiao *et al.*, 2012; Martin *et al.*, 2014).

At about 2.6 GPa, the slab transforms to eclogite with typical assemblages of garnet and clinopyroxene accompanied by chloritoid, epidote/zoisite and quartz (Poli, 1993). These are the stable sub-solidus phases until 3 GPa where epidote breaks down to leave an eclogite residue (Schmidt & Poli, 1998; Klemme *et al.*, 2002). It is thus reasonable to infer that the decoupling of Pb and Sr from other LILEs is related to the different stability conditions of their host minerals. Elevated abundances of Pb and Sr in deeper melts or fluids should thus be related to epidote breakdown in the descending slab, which had already lost a significant portion of its LILE content during previous devolatilization reactions at the depth where earlier arc and/or back-arc magmas were generated.

Another important feature of the alkaline lavas is that they are the products of partial melting of a source with greater HFSE abundances than the sources of the Phoenix Ridge and the Bransfield axial lavas (Fig. 10). Assuming that the HFSE concentrations of the source from which the most depleted axial lavas are derived represent the local convective upper mantle, the excess HFSE in the source of the alkaline melts may be interpreted to be the result of the contribution of slab melt. Thus, enrichments in both

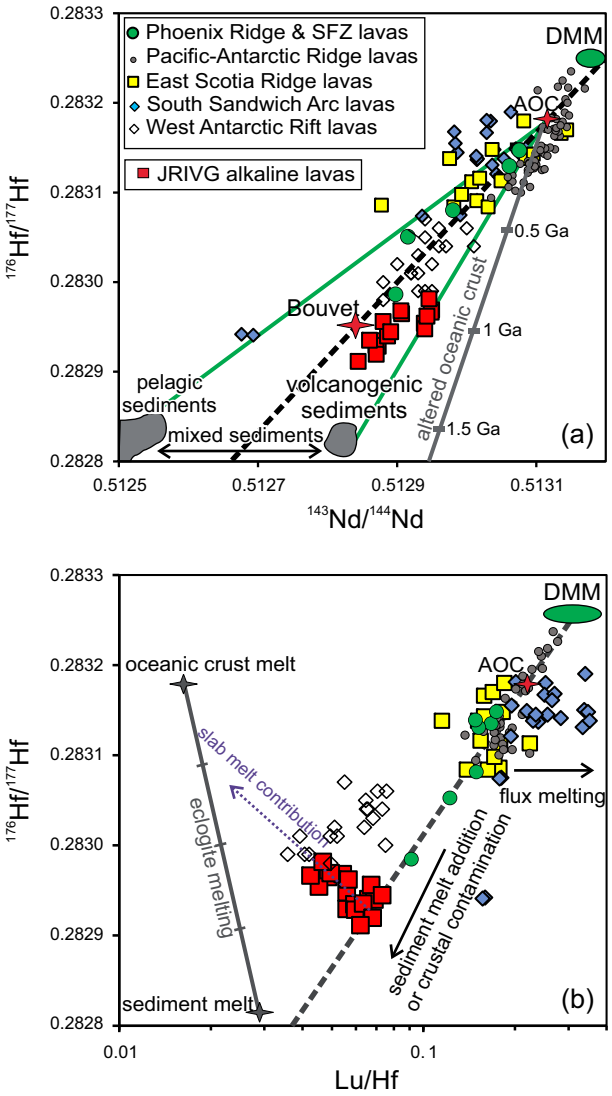

Fig. 11. a- $^{176}Hf/^{177}Hf$ vs. $^{143}Nd/^{144}Nd$; and **b-** $^{176}Hf/^{177}Hf$ vs. Lu/Hf variations for the JRIVG lavas showing the effects of slab components on the compositions of the alkaline magmas. In (a) the solid grey line represents the isotopic evolution of modeled MORB crust of varying ages generated from the depleted MORB mantle using the average present-day Lu/Hf and Sm/Nd values for N-MORB (Chauvel *et al.*, 2008, 2011), while the solid grey lines denote the addition of pelagic and volcanogenic sediments. In (b) the modelled composite slab melt is designated as the mixture of sediment and altered basaltic oceanic crust (AOC) melt assuming eclogite modal mineralogy with the parameters presented in Klemme *et al.* (2002) and Cai *et al.* (2014). The dashed line represents the mantle array. Shown for comparison are the lava compositions from the Phoenix Ridge, the Shackleton Fracture Zone, the Pacific–Antarctic Ridge, the West Antarctic Rift, the East Scotia Ridge and the South Sandwich Arc. The data sources of the lavas shown for comparison are as in Fig. 6 and 8.

LILE and HFSE are associated with slab melt hybridization during which the highly incompatible elements are all mobilized to variable extents, depending on the stability of their host minerals.

Rutile is an accessory phase in eclogite and is also the main repository of HFSE. Its sub-solidus stability restricts the mobility of HFSE by fluids or melts, resulting in relative depletion of these elements in slab components (Audetat & Keppler, 2005), while its enhanced solubility in halogen-rich aqueous fluids, supercritical fluids (Chen *et al.*, 2018), or silicate melts from warm slab melting (Hastie *et al.*, 2011) will cause increased HFSE mobility. Rutile is

likely to be a stable phase during the initial stage of subduction, but it becomes destabilized at ~3 GPa to produce a rutile-saturated melt with elevated concentrations of Ta, Nb and Ti (Klemme *et al.*, 2002). Recent studies showed that rutile solubility is increased by the presence of dissolved albite in fluids, suggesting that dissolution of rutile in eclogite containing omphacite with a high jadeite component potentially causes enhanced mobility of Nb, Ta and Ti (Gao *et al.*, 2007). The enriched LILE and HFSE patterns of the alkaline lavas should thus be the result of trace element release at pressures >3 GPa associated with progressive mineral dissolution (e.g. epidote breakdown and rutile dissolution) during subduction.

Geodynamic significance of supra-slab mantle heterogeneity

Seismic evidence suggests that the South Shetland trench is a relatively warm subduction zone that involves subduction of young oceanic lithosphere (14 to 23 Ma) with a very low convergence rate (Robertson Maurice *et al.*, 2003). The average convergence rate between the Phoenix and the Antarctic plates for the last 20 Ma has been estimated as ~24 to 75 km.myr^{-1} (Breitsprecher & Thorkelson, 2009). An *et al.* (2015) used the correlation between absolute plate motion and slab dip, and employed the parameters described in Lallemand *et al.* (2005) to suggest that subduction of the Phoenix Plate beneath the Antarctic Plate was sub-horizontal initially, but steepened gradually and was detached from the overlying Antarctic Plate with ongoing subduction as the average present-day dip angle of the slab has been estimated as ~65° (Park *et al.*, 2012). Seismic evidence also reveals a low-temperature region beneath the Antarctic Peninsula at a depth of ~150 km, interpreted as a remnant of the subducted Phoenix Plate that persists to at least 200 km depth (An *et al.*, 2015). A relatively low-velocity layer between the lithosphere-asthenosphere boundary at ~80 km and the cold relict slab most probably represents the hydrated uppermost part of the asthenosphere, and this is the likely source of the young alkaline magmas forming the JRIVG, as well as the similarly young mafic lavas of the Bransfield Basin.

In active continental margins, where an oceanic plate begins to subduct sub-horizontally in the early stages of convergence, development of the arc magma source by fluid influx takes place near the base of the continental lithosphere at some distance from the trench. Aqueous fluids released from subducted crust are enriched in large fluid-soluble cations, and interaction of such fluids with mantle wedge peridotites results in elevated concentrations of LILE and LREE in the source. Enrichments of LILE and LREE in arc lavas are probably linked to dehydration reactions that take place at lower temperatures than the wet solidus of subducted crust at sub-arc depths and produce aqueous fluids carrying high amounts of large fluid-soluble cations. Slab steepening with ongoing subduction causes trench retreat-driven extensional deformation of the overriding plate and results in partial melting of dehydrated oceanic crust at post-arc depths (Zheng, 2019). Partial melting of subducted crust of eclogitic composition at greater depths, on the other hand, produces siliceous melts enriched in all incompatible elements, and interaction of such melts with overlying peridotites generates a hybridized source that reflects the isotopic signatures inherited from both the mantle and slab components.

Melt generation in the back-arc region behind the South Shetland islands arc is likely related to lithospheric extension-driven passive upwelling which caused pressure release partial melting of the hydrated uppermost part of the mantle asthenosphere. Considering an initial lithospheric thickness of >80 km and a relatively low ratio of initial to final lithospheric thickness, however, melting requires a hot thermal profile which could be provided by lateral flow into the mantle wedge facilitated by slab rollback (e.g. Magni, 2019). This probably also provided the heat necessary for slab melting as flow-induced convective heat transfer is likely to cause slab reheating (Kimura *et al.*, 2014). Such asthenospheric flow appears to be more effective in the rear arc region beneath the Antarctic Peninsula, where the subducted slab can be efficiently heated to exceed its solidus to produce slab melts which will then ascend and react with the overlying wedge peridotites to form a hybridized source, while at sub-arc depths mantle metasomatism is related to interaction with aqueous fluids.

Melt compositions that range from subduction-enriched to intraplate-type varieties across the back-arc region thus reflect melting of distinctly metasomatized domains within the enriched mantle wedge. It is therefore reasonable to infer that the two distinct magma types in the area represent melt derivation from the aqueous fluid vs. slab melt metasomatized portions of the mantle wedge. The nature and composition of the metasomatizing agents seem to vary depending on several factors including the subduction angle and the distance from the trench, while the degree of partial melting is controlled mainly by the extent of lithospheric extension and thermal perturbation resulted from the lateral flow of mantle asthenosphere.

CONCLUSIONS

The Late Miocene to Late Pleistocene (<7 Ma) basaltic lavas exposed across the northern Antarctic Peninsula and its offlying islands are the products of alkaline magmatic activity that took place in response to lithospheric extension in the rear-arc region of the South Shetland Subduction system. The suite consists primarily of alkali olivine basalts from a series of sub-aqueous/sub-glacial and sub-aerial eruptions. The lavas display OIB-type trace element patterns indicating melt derivation from a source enriched in all highly to moderately incompatible trace elements compared to a typical MORB source. They have elevated $^{87}Sr/^{86}Sr$, $^{207}Pb/^{204}Pb$ and Th/La ratios in comparison with the local sub-lithospheric upper mantle, but they are characterized by MORB-like LILE/HFSE ratios, suggesting source enrichment by interaction with incompatible element enriched melts rather than melt contamination by crustal material. Combined evaluation of trace element and isotope systematics of the lavas suggests that the alkaline magmas are the products of partial melting of mantle wedge peridotites with imprints of metasomatic enrichment by ascending slab melt. Neodymium and Hf isotope variations further suggest that the metasomatizing agent involved is a composite slab melt originating from melting of altered basaltic crust with variable contributions from mixed sources of pelagic and volcanogenic sediments. Regional comparison of the geochemical data reveals that the upper mantle beneath the back-arc region is highly heterogeneous and contains compositionally distinct domains, reflecting the effects of both fluid influx and slab melt metasomatism.

ACKNOWLEDGEMENT

We would like to express our special thanks to the expedition members and crew of the J.G. Mendel Station for their friendship and logistic support during the field campaign (January–March 2018). We are grateful to Nadine Mattielli and Wendy Debouge for carrying out isotope analyses at the G-Time Laboratory, Université

Libre de Bruxelles (Belgium), and Irfan Yolcubal for his help with trace element analyses at the University of Kocaeli (Turkey). We would like to thank Zeynep Çalışkanoğlu for her assistance in the field, and Işıl Güraslan, Alp Ünal and Ömer Kamacı for their help with the sample preparation. Constructive reviews from Alexandre Corgne and an anonymous reviewer and helpful editorial comments from Jason Harvey are greatly acknowledged.

FUNDING

This study was supported by the Turkish Antarctic Expedition (TAE-II) program organized by the Ministry of Science, Industry and Technology (Türkiye) (grant 90220), and coordinated by Istanbul Technical University (ITU) Polar Research Center (PolReC). Field study was undertaken within the scope of TAE-II, Turkey-Czech Republic Bilateral Cooperation (grant 90220).

SUPPLEMENTARY DATA

Supplementary data are available at *Journal of Petrology* online.

References

Aldanmaz, E., Köprübaşı, N., Gürer, Ö. F., Kaymakçı, N. & Gourgaud, A. (2006). Geochemical constraints on the Cenozoic, OIB-type alkaline volcanic rocks of NW Turkey: implications for mantle sources and melting processes. *Lithos* **86**, 50–76. https://doi.org/10.1016/j.lithos.2005.04.003.

Altunkaynak, Ş., Aldanmaz, E., Güraslan, I. N., Çalışkanoğlu, A. Z., Ünal, A. & Nývlt, D. (2018). Lithostratigraphy and petrology of Lachman crags and cape Lachman lava-fed deltas, ulu peninsula, James Ross island, North-Eastern Antarctic peninsula: preliminary results. *Czech Polar Reports* **8**, 60–83. https://doi.org/10.5817/CPR2018-1-5.

Altunkaynak, Ş., Ünal, A., Howarth, G., Aldanmaz, E. & Nyvlt, D. (2019). The origin of low-ca olivine from ultramafic xenoliths and host basaltic lavas in a back-arc setting, James Ross island, Antarctic peninsula. *Lithos* **342-343**, 276–287. https://doi.org/10.1016/j.lithos.2019.05.039.

An, M., Wiens, D. A., Zhao, Y., Feng, M., Nyblade, A., Kanao, M., Li, Y., Maggi, A. & Lévêque, J.-J. (2015). Temperature, lithosphere-asthenosphere boundary, and heat flux beneath the Antarctic plate inferred from seismic velocities. *Journal of Geophysical Research Solid Earth* **120**, 8720–8742. https://doi.org/10.1002/2015JB011917.

Audetat, A. & Keppler, H. (2005). Solubility of rutile in subduction zone fluids, as determined by experiments in the hydrothermal diamond anvil cell. *Earth and Planetary Science Letters* **232**, 393–402. https://doi.org/10.1016/j.epsl.2005.01.028.

Aviado, K. B., Rilling-Hall, S., Bryce, J. G. & Mukasa, S. B. (2015). Submarine and subaerial lavas in the West Antarctic rift system: temporal record of shifting magma source components from the lithosphere and asthenosphere. *Geochemistry Geophysics Geosystems* **16**, 4344–4361. https://doi.org/10.1002/2015GC006076.

Barker, P. F. (2001). Scotia Sea regional tectonic evolution: implications for mantle flow and palaeocirculation. *Earth-Science Reviews* **55**, 1–39. https://doi.org/10.1016/S0012-8252(01)00055-1.

Barry, T. L., Pearce, J. A., Leat, P. T., Millar, I. L. & le Roex, A. P. (2006). Hf isotope evidence for selective mobility of high-field-strength elements in a subduction setting: South Sandwich Islands. *Earth and Planetary Science Letters* **252**, 223–244. https://doi.org/10.1016/j.epsl.2006.09.034.

Bédard, J. H. (2005). Partitioning coefficients between olivine and silicate melts. *Lithos* **83**, 394–419. https://doi.org/10.1016/j.lithos.2005.03.011.

Birkenmajer, K., Delitala, M. C., Narebski, W., Nicoletti, M. & Petrucciani, C. (1986). Geochronology and migration of cretaceous through tertiary plutonic centres, South Shetland Islands (West Antarctica): subduction and hot spot magmatism. *Bulletin of the Polish Academy of Sciences: Earth Sci.* **34**, 243–255.

Bizimis, M., Salters, V. J. M. & Dawson, J. B. (2003). The brevity of carbonatite sources in the mantle: evidence from Hf isotopes. *Contributions to Mineralogy and Petrology* **145**, 281–300. https://doi.org/10.1007/s00410-003-0452-3.

Boynton, W. V. (1984). Geochemistry of the rare earth elements: meteorite studies. In: Henderson, P. (ed.) *Rare Earth Element Geochemistry*. Elsevier, 63–114, https://doi.org/10.1016/B978-0-444-42148-7.50008-3.

Breitsprecher, K. & Thorkelson, D. (2009). Neogene kinematic history of Nazca–Antarctic–Phoenix slab windows beneath Patagonia and the Antarctic peninsula. *Tectonophysics* **464**, 10–20. https://doi.org/10.1016/j.tecto.2008.02.013.

Briggs, R. M. & McDonough, W. F. (1990). Contemporaneous convergent margin and intraplate magmatism, North Island, New Zealand. *Journal of Petrology* **31**, 813–851. https://doi.org/10.1093/petrology/31.4.813.

Brombin, V., Bonadiman, C., Jourdan, F., Roghi, G., Coltorti, M., Webb, L. E., Callegaro, S., Bellieni, G., De Vecchi, G., Sedea, R. & Marzoli, A. (2019). Intraplate magmatism at a convergent plate boundary: the case of the Cenozoic northern Adria magmatism. *Earth-Science Reviews* **192**, 355–378. https://doi.org/10.1016/j.earscirev.2019.03.016.

Cai, Y., LaGatta, A., Goldstein, S. L., Langmuir, C. H., Gómez-Tuena, A., Martín-del Pozzo, A. L. & Carrasco-Núñez, G. (2014). Hafnium isotope evidence for slab melt contributions in the central Mexican Volcanic Belt and implications for slab melting in hot and cold slab arcs. *Chemical Geology* **377**, 45–55. https://doi.org/10.1016/j.chemgeo.2014.04.002.

Chauvel, C., Lewin, E., Carpentier, M., Arndt, N. T. & Marini, J.-C. (2008). Role of recycled oceanic basalt and sediment in generating the Hf–Nd mantle array. *Nature Geoscience* **1**, 64–67. https://doi.org/10.1038/ngeo.2007.51.

Chauvel, C., Bureau, S. & Poggi, C. (2011). Comprehensive chemical and isotopic analyses of basalt and sediment reference materials. *Geostandards and Geoanalytical Research* **35**, 125–143. https://doi.org/10.1111/j.1751-908X.2010.00086.x.

Chen, W., Xiong, X. L., Wang, J. T., Xue, S., Li, L., Liu, X. C., Ding, X. & Song, M. S. (2018). TiO_2 solubility and Nb and ta partitioning in rutile-silica-rich supercritical fluid systems: implications for subduction zone processes. *Journal of Geophysical Research Solid Earth* **123**, 4765–4782. https://doi.org/10.1029/2018JB015808.

Coltorti, M., Bonadiman, C., Faccini, B., Grégoire, M., O'Reilly, S. Y. & Powell, W. (2007). Amphiboles from suprasubduction and intraplate lithospheric mantle. *Lithos* **99**, 68–84. https://doi.org/10.1016/j.lithos.2007.05.009.

Corgne, A., Schilling, M. E., Grégoire, M. & Langlade, J. (2018). Experimental constraints on metasomatism of mantle wedge peridotites by hybridized adakitic melts. *Lithos* **308-309**, 213–226. https://doi.org/10.1016/j.lithos.2018.03.006.

Dai, L. Q., Zhao, Z. F., Zheng, Y. F., An, Y. J. & Zheng, F. (2017). Geochemical distinction between carbonate and silicate metasomatism in generating the mantle sources of alkali basalts. *Journal of Petrology* **58**, 863–884. https://doi.org/10.1093/petrology/egx038.

Eagles, G., Gohl, K. & Larter, R. D. (2009). Animated tectonic reconstruction of the southern Pacific and alkaline volcanism at its convergent margins since Eocene times. *Tectonophysics* **464**, 21–29. https://doi.org/10.1016/j.tecto.2007.10.005.

Elizondo-Pacheco, L. A., Ramírez-Fernández, J. A., De Ignacio, C., González-Guzmán, R., Rodríguez-Saavedra, P., Leal-Cuellar, V. A., Velasco-Tapia, F. & Montalvo-Arrieta, J. C. (2022). Generation of arc-like and OIB-like magmas triggered by slab detachment in the eastern Mexican alkaline province: petrological evidence from the Cenozoic sierra de San Carlos-Cruillas complex, Tamaulipas. *Journal of Petrology* **63**, 1–24. https://doi.org/10.1093/petrology/egac027.

Elliot, D. H. (1988). Tectonic setting and evolution of the James Ross basin, northern Antarctic peninsula. *Geological Society America Memoir* **169**, 541–556. https://doi.org/10.1130/MEM169-p541.

Fretzdorff, S., Worthington, T. J., Haase, K. M., Hékinian, R., Franz, L., Keller, R. A. & Stoffers, P. (2004). Magmatism in the Bransfield Basin: rifting of the south Shetland arc? *Journal of Geophysical Research* **109**, B12208. https://doi.org/10.1029/2004JB003046.

Galer, S. J. G. & Abouchami, W. (1998). Practical application of lead triple spiking for correction of instrumental mass discrimination. *Mineralogical Magazine* **62A**, 491–492. https://doi.org/10.1180/minmag.1998.62A.1.260.

Gao, J., John, T., Klemd, R. & Xiong, X. M. (2007). Mobilization of Ti–Nb–ta during subduction: evidence from rutile-bearing dehydration segregations and veins hosted in eclogite, Tianshan, NW China. *Geochimica et Cosmochimica Acta* **71**, 4974–4996. https://doi.org/10.1016/j.gca.2007.07.027.

Gervasoni, F., Klemme, S., Rohrbach, A., Grützner, T. & Berndt, J. (2017). Experimental constraints on mantle metasomatism caused by silicate and carbonate melts. *Lithos* **282-283**, 173–186. https://doi.org/10.1016/j.lithos.2017.03.004.

Haase, K. & Beier, C. (2021). Bransfield Strait and James Ross Island: petrology. In: Smellie, J. L., Panter, K. S. & Geyer, A. (ed.) *Volcanism in Antarctica: 200 Million Years of Subduction, Rifting and Continental Break-up*. Geological Society, London, Memoirs **55**, 285–301, https://doi.org/10.1144/M55-2018-37.

Haase, K. M., Beier, C., Fretzdorff, S., Leat, P. T., Livermore, R. A., Barry, T. L., Pearce, J. A. & Hauff, F. (2011). Magmatic evolution of a dying spreading axis: evidence for the interaction of tectonics and mantle heterogeneity from the fossil Phoenix ridge, Drake Passage. *Chemical Geology* **280**, 115–125. https://doi.org/10.1016/j.chemgeo.2010.11.002.

Haase, K. M., Beier, C., Fretzdorff, S., Smellie, J. L. & Garbe-Schönberg, D. (2012). Magmatic evolution of the South Shetland Islands, Antarctica, and implications for continental crust formation. *Contributions to Mineralogy and Petrology* **163**, 1103–1119. https://doi.org/10.1007/s00410-012-0719-7.

Hamelin, C., Dosso, L., Hanan, B. B., Moreira, M., Kositsky, A. P. & Thomas, M. Y. (2011). Geochemical portray of the Pacific ridge: new isotopic data and statistical techniques. *Earth and Planetary Science Letters* **302**, 154–162. https://doi.org/10.1016/j.epsl.2010.12.007.

Hart, S. R. (1984). A large-scale isotope anomaly in the southern hemisphere mantle. *Nature* **309**, 753–757. https://doi.org/10.1038/309753a0.

Hart, S., Hauri, E. H., Oschmann, L. A. & Whitehead, J. A. (1992). Mantle plumes and entrainment. *Science* **256**, 517–520. https://doi.org/10.1126/science.256.5056.517.

Hastie, A. R., Mitchell, S. F., Kerr, A. C., Minifie, M. J. & Millar, I. L. (2011). Geochemistry of rare high-Nb basalt lavas: are they derived from a mantle wedge metasomatised by slab melts? *Geochimica et Cosmochimica Acta* **75**, 5049–5072. https://doi.org/10.1016/j.gca.2011.06.018.

Herzberg, C. & Asimow, P. D. (2015). PRIMELT3 MEGA.XLSM software for primary magma calculation: peridotite primary magma MgO contents from the liquidus to the solidus. *Geochemistry Geophysics Geosystems* **16**, 563–578. https://doi.org/10.1002/2014GC005631.

Hirose, K. (1997). Partial melt compositions of carbonated peridotite at 3 GPa and genesis of alkali basalt magmas. *Geophysical Research Letters* **24**, 2837–2840. https://doi.org/10.1029/97GL02956.

Hirose, K. & Kushiro, I. (1993). Partial melting of dry peridotites at high pressures: determination of compositions of melts segregated from peridotite using aggregates of diamond. *Earth and Planetary Science Letters* **114**, 477–489. https://doi.org/10.1016/0012-821X(93)90077-M.

Hole, M. J., Saunders, A. D., Rogers, G. & Sykes, M. A. (1995). The relationship between alkaline magmatism, lithospheric extension and slab window formation along continental destructive plate margins. *Geological Society, London, Special Publications* **81**, 265–285.

Keller, R. A., Fisk, M. R., White, W. M. & Birkenmajer, K. (1992). Isotopic and trace element constraints on mixing and melting models of marginal basin volcanism, Bransfield Strait, Antarctica. *Earth and Planetary Science Letters* **111**, 287–303. https://doi.org/10.1016/0012-821X(92)90185-X.

Keller, R. A., Fisk, M. R., Smellie, J. L., Strelin, J. A., Lawver, L. A. & White, W. M. (2002). Geochemistry of back arc basin volcanism in Bransfield Strait, Antarctica: subducted contributions and along-axis variations. *Journal of Geophysical Research* **107**, 2171. https://doi.org/10.1029/2001JB000444.

Kimura, J.-I., Gill, J. B., Kunikiyo, T., Osaka, I., Shimoshioiri, Y., Katakuse, M., Kakubuchi, S., Nagao, T., Furuyama, K., Kamei, A., Nakajima, J., van Keken, P. E. & Stern, R. J. (2014). Diverse magmatic effects of subducting a hot slab in SW Japan: results from forward modeling. *Geochemistry Geophysics Geosystems* **15**, 691–739. https://doi.org/10.1002/2013GC005132.

Klemme, S., Blundy, J. D. & Wood, B. J. (2002). Experimental constraints on major and trace element partitioning during partial melting of eclogite. *Geochimica et Cosmochimica Acta* **66**, 3109–3123. https://doi.org/10.1016/S0016-7037(02)00859-1.

Košler, J., Magna, T., Mlčoch, B., Mixa, P., Nývlt, D. & Holub, F. V. (2009). Combined Sr, Nd, Pb and Li isotope geochemistry of alkaline lavas from northern James Ross island (Antarctic peninsula) and implications for back-arc magma formation. *Chemical Geology* **258**, 207–218. https://doi.org/10.1016/j.chemgeo.2008.10.006.

Kristjánsson, L., Gudmudsson, M. T., Smellie, J. L., McIntosh, W. C. & Esser, R. (2005). Palaeomagnetic, $^{39}Ar/^{40}Ar$, and stratigraphical correlation of Miocene–Pliocene basalts in the Brandy Bay area, James Ross island, Antarctica. *Antarctic Science* **17**, 409–417. https://doi.org/10.1017/S0954102005002853.

Lallemand, S., Heuret, A. & Boutelier, D. (2005). On the relationships between slab dip, back-arc stress, upper plate absolute motion, and crustal nature in subduction zones. *Geochemistry Geophysics Geosystems* **6**, Q09006. https://doi.org/10.1029/2005GC000917.

Larter, R. D. & Barker, P. F. (1991). Effects of ridge crest-trench interaction on Antarctic-Phoenix spreading: forces on a young subducting plate. *Journal of Geophysical Research* **96**, 19583–19607. https://doi.org/10.1029/91JB02053.

Le Bas, M. J., Le Maitre, R. W., Streckeisen, A. & Zanettin, B. (1986). A chemical classification of volcanic rocks based on the total alkali–silica diagram. *Journal of Petrology* **27**, 745–750. https://doi.org/10.1093/petrology/27.3.745.

Liu, J., Xia, Q.-K., Deloule, E., Chen, H. & Feng, M. (2015). Recycled oceanic crust and marine sediment in the source of alkali basalts in Shandong, eastern China: evidence from magma water content and oxygen isotopes. *Journal of Geophysical Research, Solid Earth* **120**, 8281–8303. https://doi.org/10.1002/2015JB012476.

Livermore, R. A., Balanyá, J. C., Maldonado, A., Martínez, J. M., Rodríguez-Fernández, J., de Galdeano, C. S., Zaldivar, J. G., Jabaloy, A., Barnolas, A., Somoza, L., Hernández-Molina, J., Suriñach, E. & Viseras, C. (2000). Autopsy on a dead spreading center: the Phoenix ridge, Drake Passage, Antarctica. *Geology* **28**, 607–610. https://doi.org/10.1130/0091-7613(2000)28<607:AOADSC>2.0.CO;2.

Ma, Q. & Xu, Y.-G. (2021). Magmatic perspective on subduction of paleo-Pacific plate and initiation of big mantle wedge in East Asia. *Earth-Science Reviews* **213**, 103473. https://doi.org/10.1016/j.earscirev.2020.103473.

Machado, A., Chemale, F., Conceicao, R. V., Kawaskita, K., Morata, D., Oteiza, O. & Van Schmus, W. R. (2005). Modeling of subduction components in the genesis of the Meso-Cenozoic igneous rocks from the south Shetland arc, Antarctica. *Lithos* **82**, 435–453. https://doi.org/10.1016/j.lithos.2004.09.026.

Magni, V. (2019). The effects of back-arc spreading on arc magmatism. *Earth and Planetary Science Letters* **519**, 141–151. https://doi.org/10.1016/j.epsl.2019.05.009.

Mallik, A. & Dasgupta, R. (2013). Reactive infiltration of MORB-eclogite-derived carbonated silicate melt into fertile peridotite at 3 GPa and genesis of alkalic magmas. *Journal of Petrology* **54**, 2267–2300. https://doi.org/10.1093/petrology/egt047.

Martin, L. A. J., Hermann, J., Gauthiez-Putallaz, L., Whitne, D. L., Vitale Brovarone, A., Fornash, K. F. & Evans, N. J. (2014). Lawsonite geochemistry and stability-implication for trace element and water cycles in subduction zones. *Journal of Metamorphic Geology* **32**, 455–478. https://doi.org/10.1111/jmg.12093.

Mata, J., Martins, S., Mattielli, N., Madeira, J., Faria, B., Ramalho, R. S., Silva, P., Moreira, M., Caldeira, R., Moreira, M., Rodrigues, J. & Martins, L. (2017). The 2014–15 eruption and the short-term geochemical evolution of the Fogo volcano (Cape Verde): evidence for small-scale mantle heterogeneity. *Lithos* **288-289**, 91–107. https://doi.org/10.1016/j.lithos.2017.07.001.

Mibe, K., Kawamoto, T., Matsukage, K. N., Fei, Y. & Ono, S. (2011). Slab melting versus slab dehydration in subduction-zone magmatism. *Proceedings of the National Academy of Sciences* **108**, 8177–8182. https://doi.org/10.1073/pnas.1010968108.

Mlčoch, B., Nývlt, D. & Mixa, P. (2020) *Geological Map of James Ross Island – Northern Part 1: 25,000*. Prague: Czech Geological Survey.

Nehyba, S. & Nývlt, D. (2015). "Bottomsets" of the lava–fed delta of James Ross island volcanic group, ulu peninsula, James Ross island, Antarctica. *Polish Polar Research* **36**, 1–24. https://doi.org/10.1515/popore-2015-0002.

Nelson, P. H. H. (1975). The James Ross island volcanic group of north-East Graham Land. *British Antarctic Survey Scientific Reports* **54**.

Nývlt, D., Košler, J., Mlčoch, B., Mixa, P., Lisá, L., Bubik, M. & Hendriks, B. W. H. (2011). The Mendel formation: evidence for Late Miocene climatic cyclicity at the northern tip of the Antarctic peninsula. *Palaeogeography, Palaeoclimatology, Palaeoecology* **299**, 363–384. https://doi.org/10.1016/j.palaeo.2010.11.017.

Pankhurst, R. J. & Smellie, J. L. (1983). K–Ar geochronology of the South Shetland Islands, lesser Antarctica: apparent lateral migration of Jurassic to quaternary island arc volcanism. *Earth and Planetary Science Letters* **66**, 214–222. https://doi.org/10.1016/0012-821X(83)90137-1.

Panter, K. S., Castillo, P., Krans, S., Deering, C., McIntosh, W., Valley, J. W., Kitajima, K., Kyle, P., Hart, S. & Blusztajn, J. (2018). Melt origin across a rifted continental margin: a case for subduction-related metasomatic agents in the lithospheric source of alkaline basalt, Northwest Ross Sea, Antarctica. *Journal of Petrology* **59**, 517–558. https://doi.org/10.1093/petrology/egy036.

Park, Y., Kim, K.-H., Lee, J., Yoo, H. J. & Plasencia, L. M. P. (2012). P-wave velocity structure beneath the northern Antarctic peninsula: evidence of a steeply subducting slab and a deep-rooted low-velocity anomaly beneath the central Bransfield Basin. *Geophysical Journal International* **191**, 932–938. https://doi.org/10.1111/j.1365-246X.2012.05684.x.

Pearce, J. A. (1983) Role of the sub-continental lithosphere in magma genesis at active continental margins. In: Hawkesworth C. J. & Norry M. J. (eds) *Continental Basalts and Mantle Xenoliths, Shiva*. UK: Cheshire, pp.230–249.

Pearce, J. A., Baker, P. E., Harvey, P. K. & Luff, I. W. (1995). Geochemical evidence for subduction fluxes, mantle melting and fractional crystallization beneath the South Sandwich Island arc. *Journal of Petrology* **36**, 1073–1109. https://doi.org/10.1093/petrology/36.4.1073.

Peccerillo, A. & Taylor, S. R. (1976). Geochemistry of Eocene calc-alkaline volcanic rocks from the Kastamonu area, northern Turkey. *Contributions to Mineralogy and Petrology* **58**, 63–81. https://doi.org/10.1007/BF00384745.

Plank, T. (2005). Constraints from thorium/lanthanum on sediment recycling at subduction zones and the evolution of the continents. *Journal of Petrology* **46**, 921–944. https://doi.org/10.1093/petrology/egi005.

Poli, S. (1993). The amphibolite–eclogite transformation, an experimental study on basalt. *American Journal of Science* **293**, 1061–1107. https://doi.org/10.2475/ajs.293.10.1061.

Prouteau, G., Scaillet, B., Pichavant, M. & Maury, R. (2001). Evidence for mantle metasomatism by hydrous silicic melts derived from subducted oceanic crust. *Nature* **410**, 197–200. https://doi.org/10.1038/35065583.

Rapp, R. P., Shimizu, N., Norman, M. D. & Applegate, G. S. (1999). Reaction between slab-derived melts and peridotite in the mantle wedge: experimental constraints at 3.8 GPa. *Chemical Geology* **160**, 335–356. https://doi.org/10.1016/S0009-2541(99)00106-0.

Ringwood, A. E. (1990). Slab-mantle interactions: 3. Petrogenesis of intraplate magmas and structure of the upper mantle. *Chemical Geology* **82**, 187–207. https://doi.org/10.1016/0009-2541(90)90081-H.

Robertson Maurice, S. D., Wiens, D. A., Shore, P. J., Vera, E. & Dorman, L. M. (2003). Seismicity and tectonics of the South Shetland Islands and Bransfield Strait from a regional broadband seismograph deployment. *Journal of Geophysical Research* **108**, 2461.

Rosenthal, A., Yaxley, G. M., Green, D. H., Hermann, J., Kovács, I. & Spandler, C. (2014). Continuous eclogite melting and variable refertilisation in upwelling heterogeneous mantle. *Scientific Reports* **4**, 6099.

Sajona, F. G., Maury, R. C., Bellon, H., Cotton, J. & Defant, M. J. (1996). High field strength element enrichment of Pliocene–Pleistocene island arc basalts, Zamboanga peninsula, Western Mindanao (Philippines). *Journal of Petrology* **37**, 693–726. https://doi.org/10.1093/petrology/37.3.693.

Schmidt, M. W. & Poli, S. (1998). Experimentally based water budgets for dehydrating slabs and consequences for arc magma generation. *Earth and Planetary Science Letters* **163**, 361–379. https://doi.org/10.1016/S0012-821X(98)00142-3.

Sekine, T. & Wyllie, P. J. (1982). Synthetic systems for modeling hybridization between hydrous siliceous magmas and peridotite in subduction zones. *Journal of Geology* **90**, 734–741. https://doi.org/10.1086/628728.

Skilling, I. P. (2002). Basaltic pahoehoe lava–fed deltas: large–scale characteristics, clast generation, emplacement processes and environmental discrimination. In: Smellie, J. L. & Chapman M. G. (ed.) *Volcano–Ice Interaction on Earth and Mars. Geological Society*, London, Special Publication **202**, 91–113, https://doi.org/10.1144/GSL.SP.2002.202.01.06.

Smellie, J. L. (1987). Geochemistry and tectonic setting of alkaline volcanic rocks in the Antarctic peninsula: a review. *Journal of Volcanology and Geothermal Research* **32**, 269–285. https://doi.org/10.1016/0377-0273(87)90048-5.

Smellie, J. L. (2021). Bransfield Strait and James Ross Island: volcanology. In: Smellie, J. L., Panter, K. S. & Geyer, A. (ed.) *Volcanism in Antarctica: 200 Million Years of Subduction, Rifting and Continental Break-up*. Geological Society, London, Memoirs **55**, 227–284, https://doi.org/10.1144/M55-2018-58.

Smellie, J. L., Johnson, J. S., McIntosh, W. C., Esser, R., Gudmundsson, M. T., Hambrey, M. J. & van Wyk de Vries, B. (2008). Six million years of glacial history recorded in volcanic lithofacies of the James Ross island volcanic group, Antarctic peninsula. *Palaeogeography, Palaeoclimatology, Palaeoecology* **260**, 122–148. https://doi.org/10.1016/j.palaeo.2007.08.011.

Smellie, J. L., Johnson, J. S. & Nelson, A. E. (2013) *Geological map of James Ross Island*. I. James Ross Island Volcanic Group (1:125 000 Scale). BAS GEOMAP 2 Series, Sheet 5. Cambridge: British Antarctic Survey.

Spandler, C. & Pirard, C. (2013). Element recycling from subducting slabs to arc crust: a review. *Lithos* **170-171**, 208–223. https://doi.org/10.1016/j.lithos.2013.02.016.

Spandler, C., Hermann, J., Arculus, R. & Mavrogenes, J. (2003). Redistribution of trace elements during prograde metamorphism from lawsonite blueschist to eclogite facies; implications for deep subduction-zone processes. *Contributions to Mineralogy and Petrology* **146**, 205–222. https://doi.org/10.1007/s00410-003-0495-5.

Sun, S.-S. & McDonough, W. F. (1989). Chemical and isotopic systematics of oceanic basalts: implications for mantle composition and processes. In: Saunders, A. D. & Norry, M. J. (ed.) *Magmatism in the Ocean Basins. Geological Society*, London, Special Publication 42, 313–345, https://doi.org/10.1144/GSL.SP.1989.042.01.19.

Tatsumi, Y., Sato, K., Sano, T., Arai, R. & Prikhodko, V. S. (2000). Transition from arc to intraplate magmatism associated with backarc rifting: evolution of the Sikhote Alin volcanism. *Geophysical Research Letters* **27**, 1587–1590. https://doi.org/10.1029/1999GL008436.

Taylor, B. & Martinez, F. (2003). Back-arc basin basalt systematics. *Earth and Planetary Science Letters* **210**, 481–497. https://doi.org/10.1016/S0012-821X(03)00167-5.

Walowski, K. J., Wallace, P. J., Clynne, M. A., Rasmussen, D. J. & Weis, D. (2016). Slab melting and magma formation beneath the southern Cascade arc. *Earth and Planetary Science Letters* **446**, 100–112. https://doi.org/10.1016/j.epsl.2016.03.044.

Wang, J., Hattori, K. H., Kilian, R. & Stern, C. R. (2007). Metasomatism of sub-arc mantle peridotites below southernmost South America: reduction of fO_2 by slab-melt. *Contributions to Mineralogy and Petrology* **153**, 607–624. https://doi.org/10.1007/s00410-006-0166-4.

Wang, C., Liang, Y. & Xu, W. (2021). Formation of amphibole-bearing peridotite and amphibole-bearing pyroxenite through hydrous melt-peridotite reaction and in situ crystallization: An experimental study. *Journal of Geophysical Research: Solid Earth* **126**, e2020JB019382.

Weis, D., Kieffer, B., Maerschalk, C., Barling, J., de Jong, J., Williams, G. A., Hanano, D., Pretorius, W., Mattielli, N., Scoates, J. S., Goolaerts, A., Friedman, R. M. & Mahoney, J. B. (2006). High-precision isotopic characterization of USGS reference materials by TIMS and MC-ICP-MS. *Geochemistry Geophysics Geosystems* **7**(8), Q08006. https://doi.org/10.1029/2006GC001283.

Xiao, Y. Y., Lavis, S., Niu, Y. L., Pearce, J. A., Li, H., Wang, H. & Davidson, J. (2012). Trace element transport during subduction-zone ultrahigh-pressure metamorphism: evidence from western Tianshan, China. *Geological Society of America Bulletin* **124**, 1113–1129. https://doi.org/10.1130/B30523.1.

Yaxley, G. M. & Green, D. H. (1998). Reactions between eclogite and peridotite: mantle refertilisation by subduction of oceanic crust. *Schweizerische Mineralogische und Petrographische Mitteilungen* **78**, 243–255.

Zheng, Y.-F. (2019). Subduction zone geochemistry. *Geoscience Frontiers* **10**, 1223–1254. https://doi.org/10.1016/j.gsf.2019.02.003.

Zou, H. & Reid, M. R. (2001). Quantitative modeling of trace element fractionation during incongruent dynamic melting. *Geochimica et Cosmochimica Acta* **65**, 153–162. https://doi.org/10.1016/S0016-7037(00)00505-6.